minerals

MDPI

Article

Study of the Geological Context of the 7th–6th Century BC Phoenician Era Shipwreck "Mazarrón 2" (Murcia, Spain)

María-Teresa Doménech-Carbó [1,*], Nuria Guasch-Ferré [2], Carla Álvarez-Romero [1,3], Rocío Castillo-Belinchón [4], Soledad Pérez-Mateo [4] and Milagros Buendía-Ortuño [4]

[1] Institut Universitari de Restauració del Patrimoni, Universitat Politècnica de València, Cami de Vera s/n, 46022 Valencia, Spain; carla.alvarez.romero@gmail.com
[2] Departament d'Arts i Conservació-Restauració, Facultat de Belles Arts, Universitat de Barcelona, Carrer Pau Gargallo 4, 08028 Barcelona, Spain; nuriaguasch@ub.edu
[3] Painting Department, University of Granada, Avenida de Andalucía 27, 18014 Granada, Spain
[4] Museo Nacional de Arqueología Subacuática ARQVA, Paseo del Muelle Alfonso XII, No. 22, 30202 Cartagena, Spain; rocio.castillo@cultura.gob.es (R.C.-B.); soledad.perez.m@cultura.gob.es (S.P.-M.); milagros.buendia@cultura.gob.es (M.B.-O.)
* Correspondence: tdomenec@crbc.upv.es

Abstract: The Mazarrón 2 shipwreck was found in 1994 on the beach of Playa de la Isla (Mazarrón, Murcia, Spain). This finding is extremely important because the boat and its lead cargo were still in a reasonable conservation state and, therefore, provided new data on naval construction, commercial goods, navigation routes, and the relationships between the Phoenicians and the local population in the 7th–6th century BC. Currently, the shipwreck remains underwater, protected by a metallic coffer. In the last 2 years, a Preliminary Studies Project has been carried out, supported by national and regional public institutions. This research aims to know the shipwreck's conservation state and to determine the extraction and conservation methods at the Museo Nacional de Arqueología Subacuática ARQVA (Cartagena, Spain), where the conservation and restoration treatment will be conducted. The sampling strategy and analytical study included not only wood and other materials from the shipwreck and its cargo but also the seawater and the seabed materials in the vicinity of the shipwreck. This paper presents the results of the geochemical study of the archeological site. The applied methodology included physico-chemical tests, X-ray diffraction, optical microscopy, FTIR spectroscopy, field-emission scanning electron microscopy coupled with X-ray microanalysis, and X-ray microscopy. The results indicated that, despite the wreck being buried at a shallow depth (less than 50 cm) in a marine environment with a water column of 2–2.5 m, influenced by complex coastal dynamics that favor an oxic environment, early diagenetic processes like the formation of pyrite framboids are particularly intense in the pores and internal channels of the wreck's wood, where a different dysoxic–anoxic environment prevails. These processes have been the main mechanisms to have affected the wreck and are related to the biogeochemistry of sediments. The sediments have been confirmed to be closely related to the geological context of the Mazarrón region. The conducted study found no significant evidence of pollution due to the lead cargo.

Keywords: Mazarrón 2; shipwreck; Phoenician; waterlogged wood; conservation; pyrite framboids; marine sediment; slags; coastal dynamics

Citation: Doménech-Carbó, M.-T.; Guasch-Ferré, N.; Álvarez-Romero, C.; Castillo-Belinchón, R.; Pérez-Mateo, S.; Buendía-Ortuño, M. Study of the Geological Context of the 7th–6th Century BC Phoenician Era Shipwreck "Mazarrón 2" (Murcia, Spain). *Minerals* **2024**, *14*, 778. https://doi.org/10.3390/min14080778

Academic Editors: Marco Benvenuti and Rosarosa Manca

Received: 5 June 2024
Revised: 10 July 2024
Accepted: 25 July 2024
Published: 30 July 2024

1. Introduction

Waterlogged archeological wood can exhibit different alterations, which may occur at various degrees of severity depending on the site's environmental conditions (e.g., marine, lacustrine, marshy, etc). Shipwrecks are also preserved differently when covered by seawater or buried by seabed sediments [1]. Shipwreck deterioration occurs in the broader context of geochemical processes on the seabed regardless of the specific underwater environment.

These processes induce chemical, physical, or biological changes that characterize wood decay. The most critical geochemical processes are (a) sediment compaction; (b) bioturbation and bio-irrigation; (c) dissolution of minerals, particularly those of biogenic origin that are accompanied by exchange processes between adsorbed and aqueous cations; (d) postdepositional mobilization and migration of minerals; (e) mineral neoformation, modification, and redistribution; (f) degradation of organic matter by bacteria and the medium change from an oxidative to reductive state [2]. In addition, mineralization processes driven by microorganisms impact aquatic ecosystems [3]. Therefore, sediment diagenesis has been extensively studied in the last few decades [4–6].

Although shipwreck deterioration is associated mostly with the biogeochemistry processes involving seabed sediments and microorganisms, the current research focuses on characterizing the wood preservation state [7–25], the resultant alteration products in wood [8,12,13,15–23,26–32], and aquatic organisms and microorganisms that affect shipwreck materials [14]. Very few studies report the composition of sediments around wrecks [24,32], and no studies exist in which the geological context and geochemistry of the aquatic medium are linked with the wood alterations.

Another issue related to shipwrecks has recently drawn researchers' attention. It refers to the negative effect that the hull and ship cargo can have on the marine ecosystem as a probable source of heavy metal pollution [33].

This study focuses on the Mazarrón 2 wreck, found in 1994 on the beach of Playa de la Isla in Mazarrón (Murcia, Spain) in shallow maritime waters (Figure 1). The wreck is currently buried at a shallow depth (water column at ca. 2–2.5 m). The ownership of this site is the Comunidad Autónoma de la Region de Murcia (CARM; the Spanish Autonomous Community of Murcia Region), which declared the site an "Asset of Cultural Interest" (BIC, Spanish acronym) in the Archeological Zone category in 2015. This finding is extremely important because the boat and its lead cargo were still in a reasonable conservation state and, therefore, provided new data of archeological interest. In 2000, the shipwreck was excavated, and its cargo and other objects were recovered, but the wooden boat remains are in situ buried and protected by a metallic coffer (Figure 2) [34–36]. The study of the wreck's geological context, which is presented in this paper, is part of a Preliminary Studies Project that began in 2022 and is supported by the Ministerio de Cultura de España (MCU; the Spanish Ministry of Culture) and CARM. These studies have focused on assessing the shipwreck's conservation status prior to making further decisions about its future management [37]. This Preliminary Studies Project has been structured as a coordinated and interdisciplinary effort that involves the different specialists responsible for recording and documenting the wreck [38] and for designing an appropriate sampling strategy to study wood deterioration, marine sediments, and seawater composition [39]. The Preliminary Studies Project results are essential for developing a proyect draf, which must be reviewed and validated by international experts and national managers. Then, the validated preliminary draft should serve as a guide for the future management plan for Mazarrón 2, including raising methodologies and remediative conservation tasks at the Museo Nacional de Arqueología Subacuática ARQVA (National Museum of Underwater Archeology, Cartagena, Spain) and long-term research, remediative/preventive conservation, and public dissemination efforts related to the shipwreck [37].

This study presents the geochemical findings of the site and correlates them with the wreck wood analysis to identify the alteration processes that affect the current preservation state of Mazarrón 2. The applied methodology included physico-chemical tests, X-ray diffraction, FTIR spectroscopy, optical microscopy, field-emission scanning electron microscopy–X-ray microanalysis (FESEM-EDX), and X-ray microscopy (XRM).

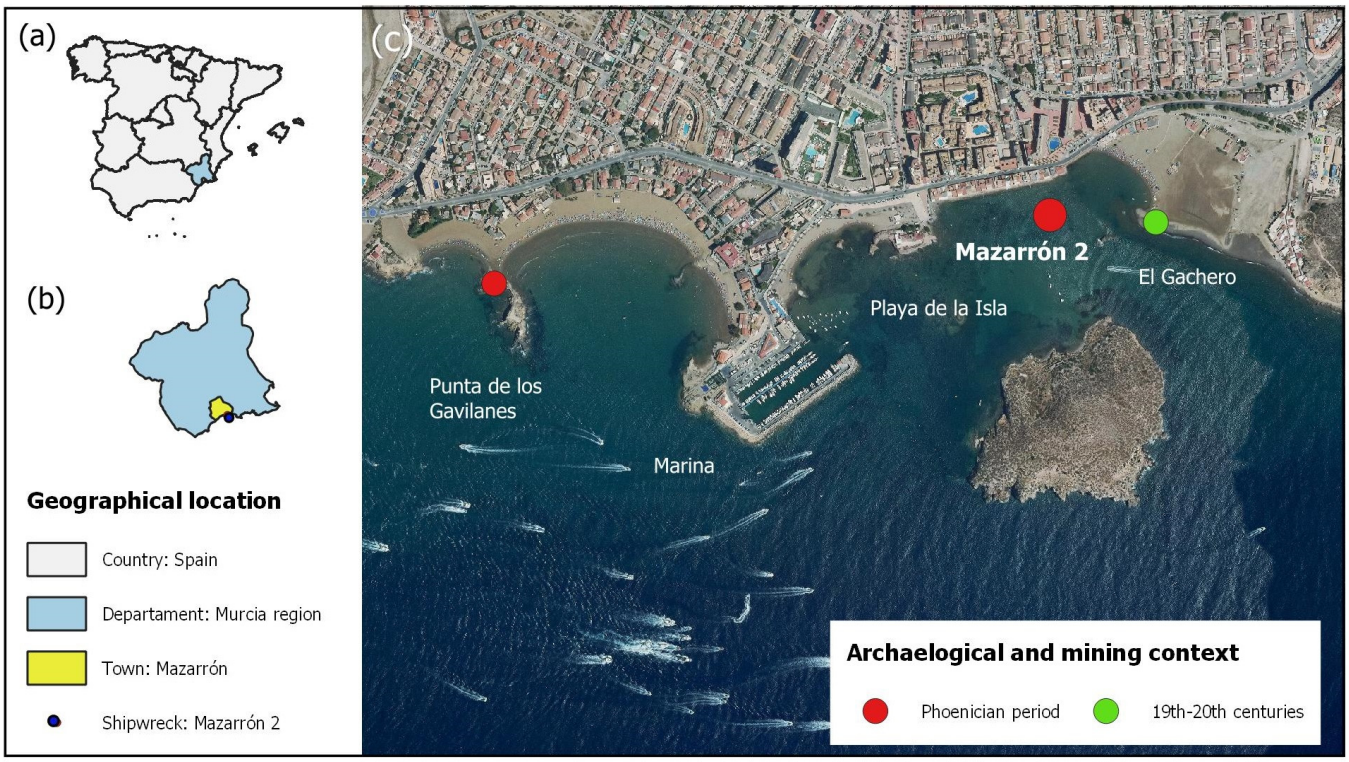

Figure 1. Location of the Mazarrón 2 shipwreck in the Murcia Region (Spain) and its archeological and mining contexts. (**a**) The Murcia Region in Spain; (**b**) the Mazarrón district in the Murcia Region; (**c**) a photograph of the Mazarrón 2 site. Red dots show Punta de los Gavilanes and the Mazarron 2 shipwreck archeological sites from the Phoenician period. The green dot denotes the El Gachero embankment on the El Rincón de Playa de la Isla. Photographs are from the open access database of the Instituto Geográfico Nacional de España (Spanish National Geographic Institute): general maps (**a**,**b**) and orthophoto PNOA 2022 (**c**); figure assembled by Rocío Castillo-Belinchón.

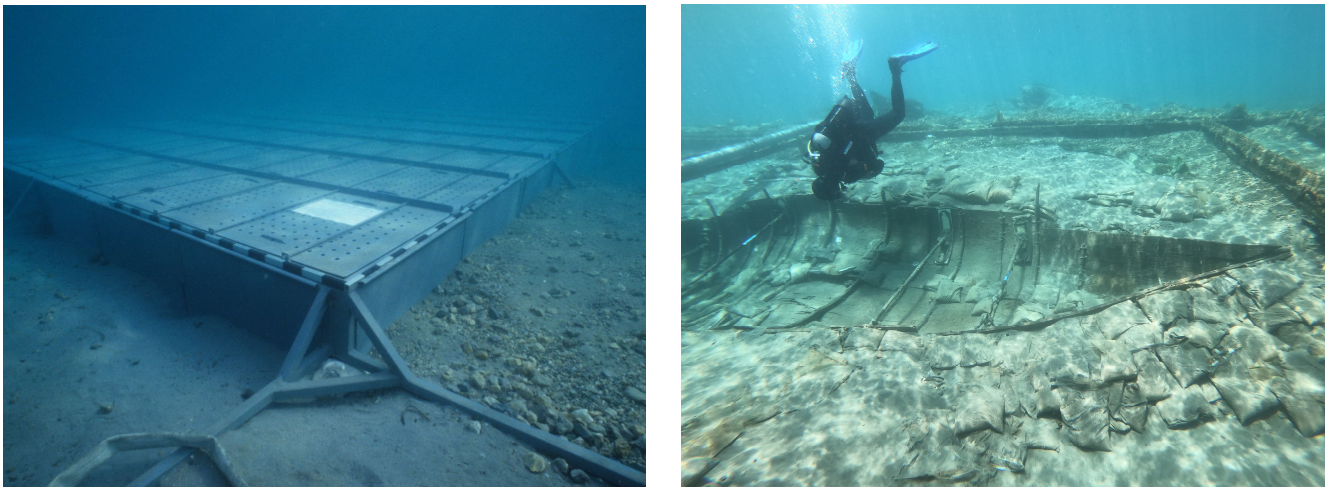

(**a**) (**b**)

Figure 2. (**a**) Metallic coffer used for the wreck's in situ protection since 1999; (**b**) image of Mazarrón 2 during works in June 2023 (photographs by Pedro Ortiz (**a**) and Milagros Buendía-Ortuño (**b**) archive of the Museo Nacional de Arqueología Subacuática).

2. Historical and Geographical Setting

Mazarrón 2 is a small ship (8.15 m long × 2.20 m beam and a minimum depth of 0.9 m) built in wood, whose hull is almost entirely conserved. The ship carried a cargo of 2800 kg of lead ingots, along with various objects that witnessed life on board (e.g., a stone hand mill, a basket of sparto grass, and remains of animal bones) [36,40]. A wooden anchor with lead stocks close to the hull is considered the oldest example of this type of anchor throughout the Mediterranean [36,41]. These findings document shipbuilding and shipping routes in the first half of the 1st millennium BC. They are also a testimony of the exploitation of metals by the Phoenicians in the Iberian Peninsula [36]. Recent studies on naval shipbuilding suggest that Mazarrón 2, together with Mazarrón 1, another wreck found nearby, are the oldest examples of naval shipbuilding of Phoenician origins found on the Mediterranean coast of the Iberian Peninsula [42,43]. These studies on shipbuilding techniques, especially the latest studies on the anchor, confirm that Mazarrón 2 is a ship from the Phoenician period and allow more specific dating between the end of the 7th century BC and the first third of the 6th century BC [36–38,44–46].

The Mazarrón 2 shipwreck is linked with the local mining context. The lead isotope analysis of the Mazarrón 2 cargo suggests that it comes from the mining districts of Cartagena and Mazarrón [47]. The Mazarrón mining region covers an area of 7 km^2 around the city of Mazarrón. Since ancient times, this region has been rich in metal deposits, copper, iron, silver, lead, and alum. The area includes three main mining sites, San Cristobal-Los Perules, Pedreras Viejas, and Coto Fortuna, exploited during various periods and separated by phases of inactivity from antiquity to the 1960s [48–50]. Two other local archeological sites, located 5 km away from the above-mentioned mining sites and dating back to the Phoenician era, from the same historical period of Mazarrón 2, might be related: Punta de los Gavilanes and Playa de la Isla (Rincón de la Isla) (Figure 1). In the Phoenician enclave of Punta de los Gavilanes (Cabezo del Gavilán) on Playa Bahía, located 1 km away from the Mazarrón 2 shipwreck, archeologists have found remains of the oldest silver cupellation workshop in the Murcia Region, including cupels, silver, lead, and slags [51]. In the anchorage of Playa de la Isla, primarily used in Phoenician times and where shipwrecks Mazarrón 1 and 2 were found, noticeable archeological remains include some lead ingots, a silver scarab, the handle of an iron-rich bronze lance, and abundant fragments of Phoenician ceramics, which indicate the presence of a sophisticated kiln [52].

Mazarrón 2 is located some 500 m away from Santa Elisa's lead-smelting factory. It operated between 1886 and 1927 and was the first lead-smelting factory in Spain. By-product slags were discarded at the Rincón de la Isla, 200 m away from Mazarrón 2, and gradually formed an embankment called El Gachero. This embankment grew progressively along the Playa de La Isla shoreline [53,54]. The sandy barrier formed in El Gachero significantly altered the local marine coastal dynamics at Playa de la Isla (Figure 3). The central area slowly eroded, while loose sand accumulated in the coastal shelter formed in El Gachero, located in the eastern sector of the beach. In the 1980s, the construction of a nearby marina in the western area of Playa de la Isla negatively influenced the coastal dynamics and contributed to the increased erosion of the central part of the beach where Mazarrón 1 and Mazarrón 2 are located [55,56]. These active coastal processes allowed archeological remains in the area to be discovered in the 1980s and 1990s. However, they currently pose a threat to the in situ conservation of the Mazarrón 2 wreck. As a result, the MCD and CARM have agreed to raise the ship, but not before conducting the Preliminary Studies Project, which includes the study of the geochemical context presented in this paper.

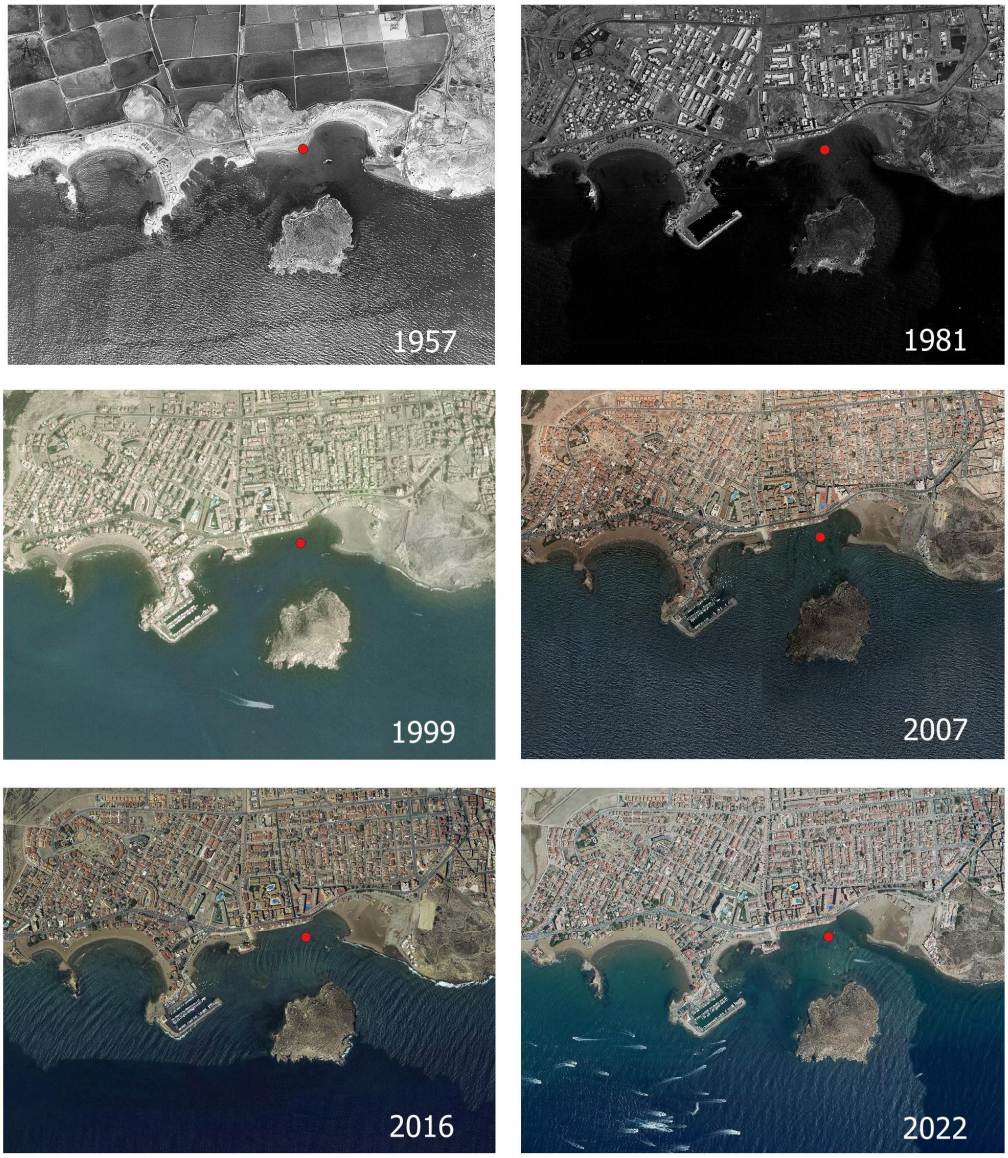

Figure 3. Evolution of the coastal dynamics and profile of Playa de la Isla, with the Mazarrón 2 shipwreck marked by a red dot, and reflected in this aerial photographs series: 1957, American flight (USAF); 1981 regional flight (CARM); 1999, 2007, 2016, and 2022 national orthophotos (PNOA—IGN) (assembled by Rocío Castillo-Belinchón with free access images available at the CARM and the Instituto Geográfico Nacional.

3. Materials and Methods

3.1. Sampling

The sampling strategy for the Preliminary Studies Project was carefully planned to achieve complete process traceability. The sampling strategy enabled the correct identification of the sample type (seawater, sediment, cargo, wood hull, life-on-board things, etc.) by assigning a standardized inventory code according to the protocol for receiving the underwater materials developed at the ARQVA since 2011 (Table S1 provided as Electronic Supplementary Materials). The first four characters of standard code MZB2 identify the place (MZ = Mazarrón) and the site (B2 = boat 2), followed by several characters that correspond to the year and sampling point. This methodology contrasts with previous samplings of the cargo and life-on-board objects authorized by the CARM, which were noted for their bias [37].

Eighteen sediment samples were recovered from the archeological site. The 16 referred to in this paper, from MZB2-01 to MZB2-16, were recovered in an area of 16 × 26 m surrounding Mazarrón 2 (Figure 4). The other two samples were recovered from El Gachero (Playa de la Isla) (MZPI-01) and Cabezo del Gavilán (Playa Bahía) (MZCG-01) (Figure 1). Two wood samples, labeled MAZ-01 and MAZ-02, were recovered from the wreck (Figure 4). The complete sample list, references, and details of the sampling points are provided in Table S1. Sample MZB2-14 was used for an archeological study that is not reported in this paper.

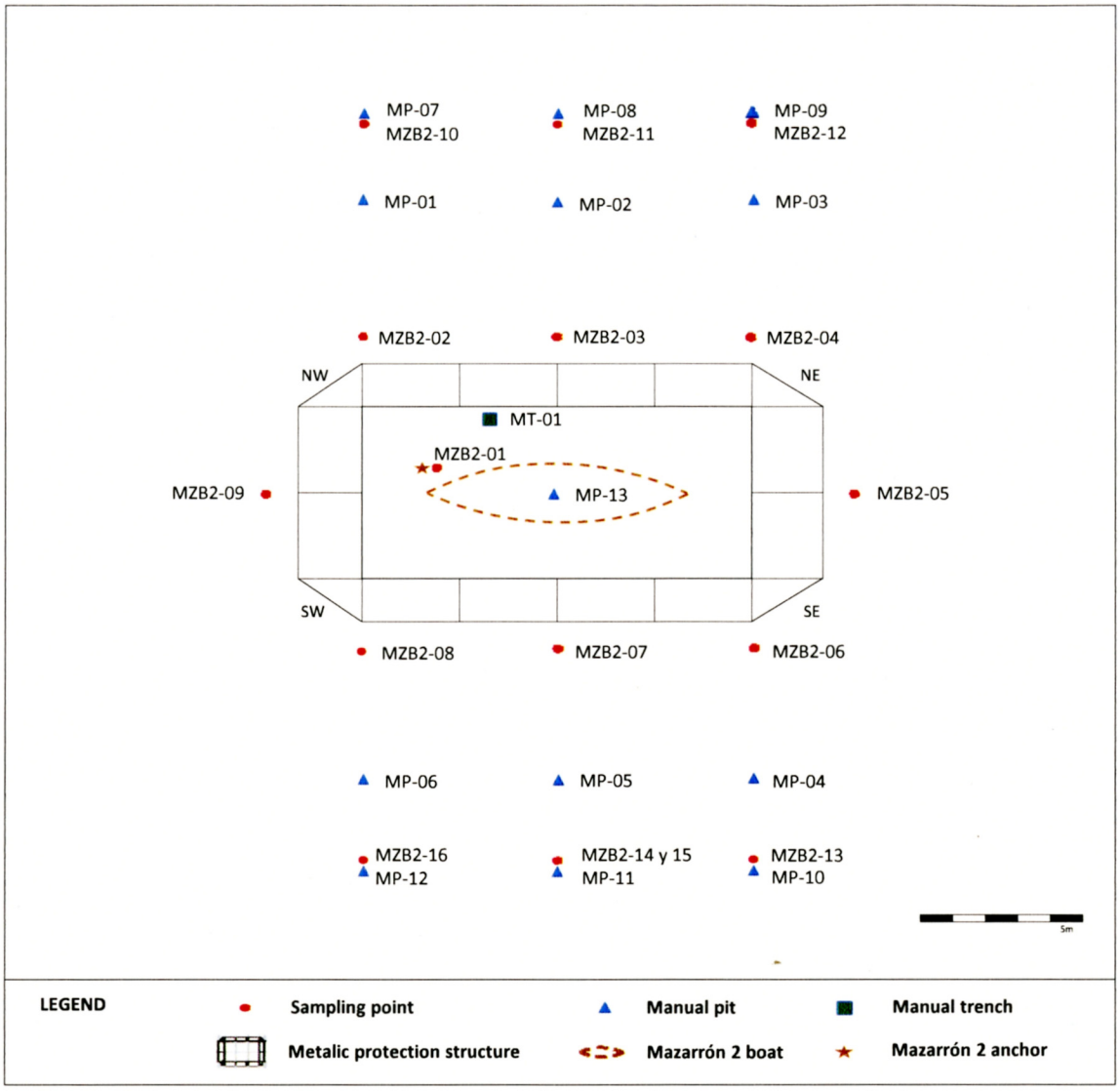

Figure 4. Distribution of sediment sampling points (MZB2-01 to MZB2-16, MZPI-01 and MZCG-01), measurement points (MP-01 to MP-12), and manual trench MT-01 around the Mazarrón 2 shipwreck in June 2023 (Drawing made by Rocío Castillo-Belinchón y Nuria Guasch-Ferré).

Manual excavation pits, made with a small shovel, were used for sediment sampling purposes to avoid subjecting the wreck to unnecessary vibrations. The sample from under the anchor (MZB2-01) was collected at approximately 80 cm (−80 cm) below the seafloor surface. The remaining samples, both those collected in the vicinity of the shipwreck (MZB2-02 to MZB2-09) and those collected within 10 m of the shipwreck (MZB2-10 to MZB2-16), were taken at about 20–30 cm and (−20)–(−30) cm from the seafloor surface. In all these cases, the bathymetry of the seafloor was approximately 2 m.

The samples from the other two extraction sites were taken on the seafloor surface, very close to the shore: MZPI-01 (Playa de la Isla) and MZCG-01 (Cabezo del Gavilán). In these two cases, the bathymetry of the seabed was approximately 1 m.

The sediment samples were airtight-sealed and frozen to preserve their original composition and to prevent any potential deterioration. They were conserved in a refrigerator until the sediment analyses were carried out. The wood samples were conserved in seawater to maintain their moisture content and to prevent drying. They were placed inside sealed flasks in a refrigerator at 3 °C. Prior to the different instrumental analyses, the sediment subsamples were dried to a constant mass in a laboratory oven to ensure accurate measurements.

3.2. Instrumentation

The instruments and operating conditions are provided in Table S2. The laboratory methods included the following:

(1) Optical microscopy: The sediments and wood samples were directly examined under an optical microscope. The sediment samples consisted of dried sand–silt–clay dispersed with a thin needle on a glass slide.

(2) Scanning electron microscopy-X-ray microanalysis: The same subsamples examined under an optical microscope were mounted on aluminum disks and carbon-coated before acquiring images and X-ray spectra. A second series of sediments were finely powdered in an agate mortar and mounted on aluminum discs to perform the quantitative elemental analysis. The ZAF method of correction of the interelemental effects on intensity values was applied in each X-ray spectrum for every element. Three X-ray spectra from an area of 2.4 × 2.4 mm were acquired on three replicates of each sediment. The oxide wt% values of the different elements were calculated using the AztecOne software.

A third series of subsamples were prepared as cross-sections. A small amount of sediment was embedded in polyester resin (Glasspol 328, Glasspol Composites SL, Valencia, Spain) and polished with abrasive dishes of SiC (Struers, Champigny sur Marne, France) until a uniform cross-section was obtained. The X-ray spectra acquired from these specimens enabled the characterization of the mineral composition of individual grains to avoid the interfering effect of the NaCl microcrystals deposited on the surface during drying in the laboratory (Figure S1). The stoichiometry of the mineral is deduced from the molar ratio among the identified elements, which is provided by the quantitative processing of the detected X-ray counts.

(3) FTIR spectroscopy: sediments and wood subsamples were finely powdered in an agate mortar.

(4) X-ray diffraction: sediment subsamples were finely powdered in an agate mortar.

(5) X-ray microscopy: dried wood fragments of a few mm were examined by an X-ray microscope.

3.3. Physical Tests

3.3.1. Density

The basic density (BD) and maximum water content (MWC) were calculated for the wood samples following the method described elsewhere [9,10].

3.3.2. Sediment Color Determination

The color of the marine sediments was determined using the Munsell Soil Color Chart (version 2009) [57]. Samples were air-dried and evaluated under natural light. The resulting color annotations, such as the hue, value, and chroma, were noted in the log with the sample code [58].

3.3.3. Granulometric Analysis

The samples' particle size distribution (PSD) was determined using a set of laboratory test sieves. Thirteen groups of sediment grain sizes were measured from a silt and clay size of <0.063 mm to a pebble >4 mm [6,59–61]. Analyses were conducted with 100 ± 2 g of each sample. Sedimentary textures and their corresponding terminology were determined according to the Unified Soil Classification System (USCS) [62]. Granulometric fractions (gravel + sand + mud), statistical parameters defined by Folk and Ward [63] and Royse [64], and the coefficient of uniformity (C_u) and curvature (C_c) used to classify soils were calculated. These parameters are related to the effective sizes (D_{10}), (D_{30}), and (D_{60}), which represent the characteristics of the PSD curve in terms of the shape factors [60,62,65].

3.3.4. Geotechnical Characterization of the Seabed

In parallel to the sampling, geotechnical measurements were taken to assess the physical properties of the seabed using Jacob's Staff (a –1.5 m length metal staff marked every 10 cm) to avoid subjecting the wreck to unnecessary vibrations. The 13 measurement points—labeled MP-01 to MP-13—are shown in Figure 4. Additionally, a bigger pit or manual trench (MT-01 in Figure 4) was made to record the stratigraphy of the geological substrate at the site next to the shipwreck. The manual trench was made with dredge pumps used in archeological excavations. The trench dimensions were 50 cm^2 in area and −150 cm in depth, counted from the bottom of the shipwreck (Figure 5).

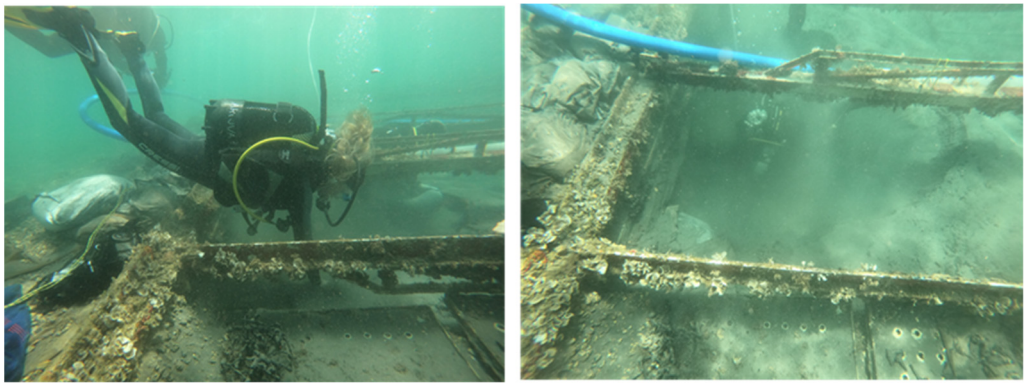

Figure 5. Manual trench (MT-01) inside the metallic protection structure, northwest of the shipwreck, during works in June 2023 (**Left**); detail of the prior image (**Right**) (Photographs by Rocío Castillo-Belinchón, Archive of the Museo Nacional de Arqueología Subacuática).

3.4. Degree of Pyritization

The degree of pyritization (DOP) was calculated according to the theoretical model and experimental procedure described elsewhere [66–69]. The concentration of the metal in aqueous extracts was spectrophotometrically determined [70]. DOP provides not only a measure of the amount of pyrite present in the samples but also an estimate of the oxygen levels [71,72], where:

- Normally oxygenated (oxic) environment: DOP < 0.45;
- Oxygen-restricted (dysoxic) environment: DOP ranges 0.4 < DOP < 0.7;
- Oxygen-depleted (anoxic to euxinic): DOP > 0.7.

4. Results

4.1. Topography of the Seabed

The obtained results (Table S3 and Figure 4) determined that the wreck does not sit directly on a rocky substrate, as at all the measured points. A sandy sediment layer was found, which varied from a −20 cm to −68 cm depth, depending on the checked point. The manual pits also indicated that, on the outermost sandy layer of depths of a few cms, the sediment was influenced by water recirculation. As it deepened, and depending on the

measurement point, sediment became more resistant to staff penetration, which suggests the material's higher density. The values summarized in Table S3 also show how a thicker sediment layer tends to appear at the south-oriented measurement points. These latter results were confirmed in the manual trench (MT-01). In this case, a succession of sandy sediment layers of different densities was documented, but no rocky substrate was found.

4.2. Characterization of Sediments

4.2.1. Physical Properties

Three properties were considered to be representative of the physical properties of the sediments: color, grain size distribution, and grain morphology.

The near-wreck sediments MZB2-02 to MZB2-16 and MCGC-01, taken immediately below the sediment–water interface, looked brownish. The deepest sample, MZB2-01, taken from under the anchor, was gray. The El Gachero sediment was darker and reddish brown (Figure 6a). Under the optical microscope, most of the grains were translucent, bright, and opaque, with a wide range of hues varying from black to white, gray, yellowish, reddish, ochre, sienna, brown, and green. All the grains seemed to be dyed orange, probably due to the deposition of iron oxides and oxyhydroxides (Figure 7a,b).

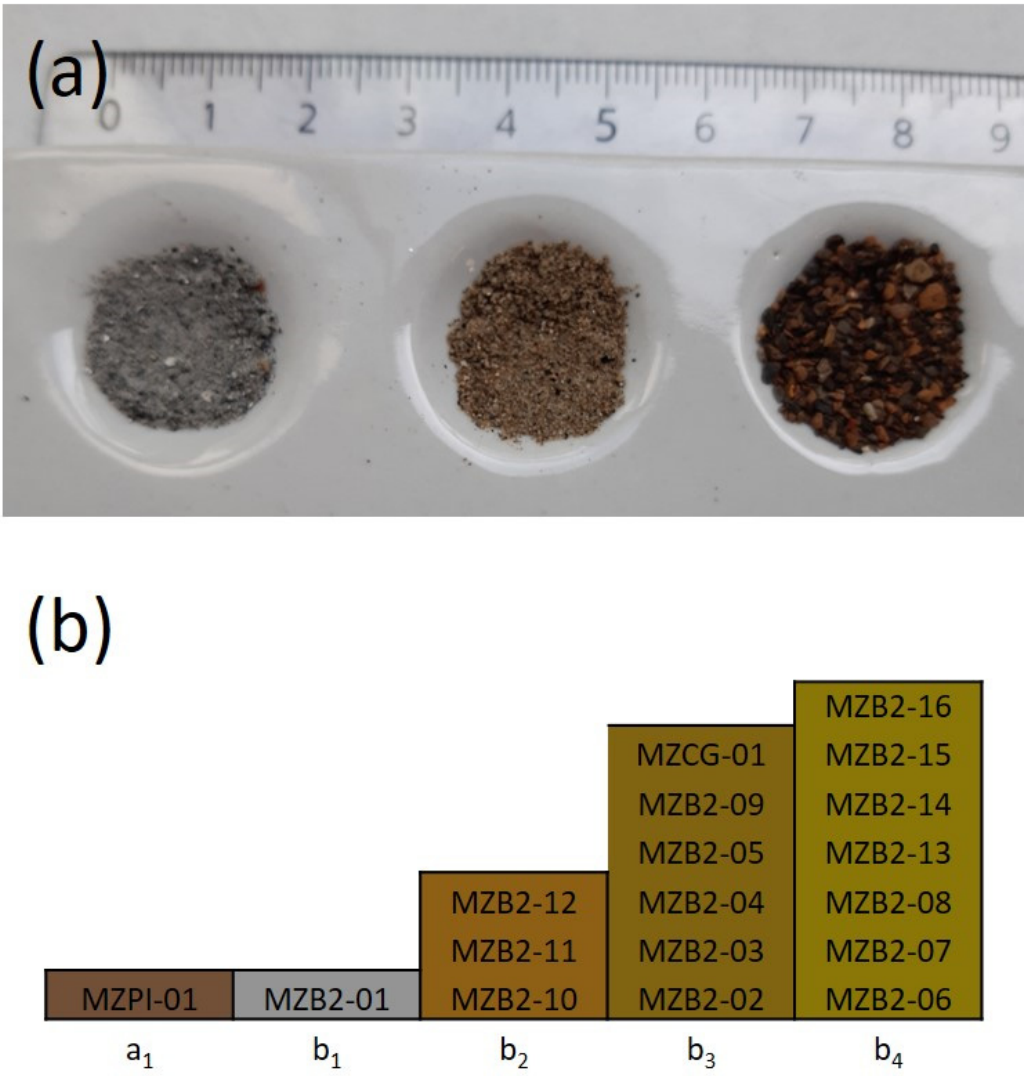

Figure 6. (**a**) Photograph of sediments MZB2-01 (**left**), MZB2-02 (**middle**), and MZPI-01 (**right**); cm scale. (**b**) Classification of sediment samples according to their color.

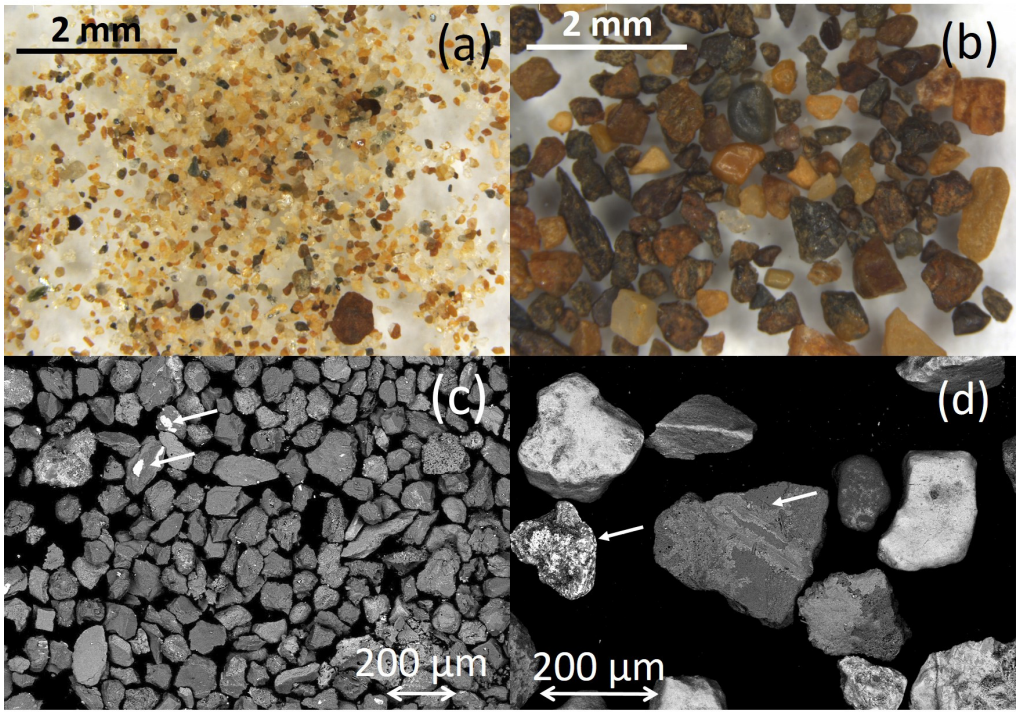

Figure 7. Photographs of the dried sediments obtained by using a stereoscopic microscope operating with episcopic illumination: (**a**) MZB2-09 and (**b**) MZPI-01. Backscattered electron images of the sediments, acquired with FESEM at 20 kV: (**c**) MZB2-01 and (**d**) MZPI-01. Arrows point out the microcrystalline deposits of formed NaCl on the grains' surface during laboratory drying of the sediment samples.

According to the Munsell Chart, all the samples belong to the 10YR Hue category, a yellowish hue corresponding to 10 parts yellow to 1 red. The sediments were classified into five different color types, depending on their lightness and saturation, as follows [73]: type a_1 (10YR 5/4), yellowish brown; type b_1 (10YR 6/1), gray; type b_2 (10YR 6/2), light brownish-gray; type b_3 (10YR 6/3–6/4) pale brown-light yellowish brown; type b_4 (10YR 6/6) brownish yellow (Figure 6b and Table S4).

Two color trends of depth and orientation were recognized. A significant color difference was observed between the sediments MZB2-15 and MZB2-01, taken at depths of 20–30 and 80 cm, respectively (Figure 6a). Second, a progressive increase in darkness was also recognized when the sediments passed from north to south.

The optical and electron microscopy images shown in Figure 7a,c (samples MZB2-09 and MZPI-01) represent the grain morphology of the wreck surroundings' sediments. Near-wreck sediments are composed of grains primarily comprised within the sand range. Under an optical microscope, most grains fell within the range of coarse sand to fine graves. The subangular to a rounded shape and the scarce to fine superficial roughness denote their terrigenic origin and the erosive processes undergone during their diagenesis. Biogenic materials were easily identified in all the examined samples. They were micro-fragments of skeletons of small-sized marine organisms (gastropods, echinoderms, diatoms, among others). Sample MZPI-01 from El Gachero differed from the near-wreck samples by having larger grains (Figure 7b,d).

The grain size classification of the analyzed sediments was based on the Wentworth scale [74]. When analyzing the fine fraction was not possible, the binary based on the sand-to-mud (silt + clay) ratio was applied [75]. About 60% of the studied samples were composed of fine sands, with a 0.125 mm preferred grain size, and the remaining 40% were divided between the medium sands (0.250 mm preferred grain size) and fine gravels (>2 mm preferred grain size) (Table S5). The percentages of gravels, sands, and fines of sediments were calculated from the PSD curves (Figures S2 and S3 and Table S5). In this

case, ca. 60% of the studied sediments obtained a value of >95% of sand, corresponding to fine sands, and the very coarse and very fine fractions represented a <5% retention. The D_{10}, D_{30}, and D_{60}, and C_c and C_u parameters calculated from the PSD curve are also shown in Table S5.

Four different sediment groups (I to IV) were distinguished. Group I included samples MZB2-01 to MZB2-05, MZB2-07, MZB2-08, MZB2-11 to MZB2-16, and MZCG-01. They were poorly graded sediments, from medium to fine sandy, corresponding to the sand with gravel (SP) class, according to the USCS. Three subgroups were distinguished here according to the PSD. Subgroup I_a included poorly graded sandy samples MZB2-02 to MZB2-04, MZB2-13 to MZB2-16, and MZCG-01 (Figure S2). Subgroup I_b comprised the MZB2-01, MZB2-07, MZB2-08, and MZB2-12 samples of the SP class composed of poorly graded sand with gravel. The subgroup I_c MZB2-05 and MZB2-11 samples were composed of poorly graded sand with silt and gravel sediments (SP SM). Subgroups I_b and I_c presented bigger particles, most of which were micro-fragments of skeletons of marine organisms. In the I_b sediments, the gravel percentage was 2–6%, and the sediments in the I_c subgroup varied between 9% and 11%. Groups I_a and I_b exhibited unimodal distribution with negative asymmetry on the PSD curve, which indicates a very uniform size distribution. The values of $C_u < 6$ and C_c, beyond the 1–3 range, suggested poorly graded sediments. The I_c subgroup exhibited a bimodal preferential curve that was distributed between fine sand (0.125 mm) and fine gravel (4 mm), which implies that these sediments were a mixture of materials.

Group II was composed of MZB2-09 and MZB2-10, which were silty sand with fine gravel, and the USCS notation SM (silty sand with gravel). The amount of gravel in these two samples fell within the 17–21% range. The PSD curves exhibited a bimodal preferential profile with a mixture of poorly graded fine sand grains (0.125 mm) and fine gravel (4 mm) (Figure S3).

Group III included the sediment sample MZB2-06, composed of fine gravel with sand and silt, labeled poorly graded gravel with silt and sand (GP GM), according to the USCS. The PSD curve, shown in Figure S3), exhibited trimodal preferential distribution with fine sand (0.125 mm), coarse sand (0.5 mm), and fine gravel (4 mm). All this indicates a mixture of materials poorly graded with $C_u > 4$ and C_c beyond the 1–3 range.

Finally, sediment MZPI-01 was included in Group IV, formed by silty gravel with sand materials (GM). The PSD curve showed polymodal preferential distribution with fine (0.125 mm), medium (0.250 mm), coarse (0.5 mm), and very coarse (1.25 mm) sand, as well as fine gravel (4 mm). This suggests a mixture of different types of well-graded materials (Figure S3).

4.2.2. Chemical and Mineralogical Composition

The chemical composition of the sediments is shown in Table 1. The results obtained from the sediments found in the surroundings of the wreck (MZB2-@ series) and on Cabezo del Gavilán (Bahía beach) (MZCG-@) suggest that sediments were formed mainly by terrigenic minerals, such as quartz, aluminosilicates, clayey minerals, and biotite (40.1–52 SiO_2%, 5.8–10.2 Al_2O_3%). The sodium and potassium values within the 2.1–3.5 Na_2O% and 1.6–2.63 K_2O% ranges were associated primarily with alkaline feldspars. Halite was also identified in all the samples associated with microcrystals, probably deposited on the surface of grains during sediment drying (Figure 7c,d). The high calcium contents and, to a lesser extent, of magnesium were due to the abundance of calcite and Mg-calcite, both of terrigenic and biogenic origins (14.2–34.4 CaO%, 3.5–7.7 MgO%). Titanium within the 0.2–1.0 TiO_2% range was associated with terrigenic ilmenite, titanite, and titanomagnetite. The sulfur content of 0.3–1.6 SO_3% was ascribed to pyrite and related minerals that take part in redox processes. The iron content of 4.6–9.9 FeO% was primarily ascribed to the presence of terrigenic minerals, such as micas, clays, iron oxides, and chemogenic iron, that take part in the redox iron cycle in the sea. The sediment from Cabezo de Gavilán, located in the ancient port where the mineral from mines was loaded onto ships, also included some zinc and manganese. The El Gachero MZPI-01 sample exhibited

notable compositional differences. This sample had the highest CaO (35%), FeO (22.4%), MgO (8.4%), and SO_3 (2.5%) contents. Manganese, copper, zinc, lead, and barium were also present at minor/trace levels. These elements were related to the mining by-product slags that formed El Gachero.

Table 1. Chemical composition (oxide wt %) obtained using FESEM-EDX in the studied sediments; standard deviations in brackets.

Oxide	MZB2-01	MZB2-02	MZB2-03	MZB2-04	MZB2-05	MZB2-06	MZB2-07	MZB2-08	MZB2-09
Na_2O	3.1 (0.9)	3.2 (0.2)	3.41 (0.03)	3.2 (0.3)	3.4 (0.3)	2.1 (0.1)	3.4 (0.1)	2.2 (0.3)	2.1 (0.2)
MgO	4.9 (0.5)	4.6 (0.2)	5.0 (0.2)	4.37 (0.06)	5.2 (0.3)	6.0 (0.5)	5.1 (0.2)	5.8 (0.2)	6.0 (0.1)
Al_2O_3	8.3 (0.7)	10.4 (0.1)	9.68 (0.07)	10.4 (0.7)	9.5 (0.3)	5.8 (0.3)	8.2 (0.3)	6.8 (0.1)	8.9 (0.4)
SiO_2	53 (1)	46.3 (0.9)	42 (2)	43 (2)	42.3 (0.5)	50 (2)	47 (1)	47 (1)	44.4 (0.5)
SO_3	1.5 (0.3)	0.3 (0.5)	1.4 (0.2)	n.d.	1.6 (0.3)	0.7 (0.6)	1.1 (0.2)	0.7 (0.2)	1.2 (0.2)
K_2O	1.9 (0.1)	2.63 (0.04)	2.6 (0.1)	2.6 (0.1)	2.6 (0.1)	1.6 (0.1)	2.1 (0.2)	1.8 (0.1)	2.2 (0.1)
CaO	21 (1)	21.2 (0.1)	24 (2)	23 (2)	24.3 (0.3)	27 (1)	24.7 (2)	27.6 (0.8)	26.8 (0.6)
TiO_2	0.6 (0.1)	0.8 (0.1)	0.7 (0.3)	1.0 (0.5)	0.6 (0.1)	0.3 (0.3)	0.4 (0.3)	0.6 (0.2)	n.d.
MnO	n.d.	n.d.	n.d.	n.d.	n.d.	n.d.	n.d.	n.d.	n.d.
FeO	3.4 (0.2)	8.5 (0.2)	8.25 (0.03)	9.9 (0.2)	7.8 (0.2)	5.5 (0.2)	4.8 (0.4)	5.6 (0.2)	6.7 (0.2)
CuO	n.d.	n.d.	n.d.	n.d.	n.d.	n.d.	0.2 (0.2)	n.d.	n.d.
ZnO	n.d.	n.d.	n.d.	n.d.	n.d.	n.d.	n.d.	n.d.	n.d.
PbO	n.d.	n.d.	n.d.	n.d.	n.d.	n.d.	n.d.	n.d.	n.d.
BaO	n.d.	n.d.	n.d.	n.d.	n.d.	n.d.	n.d.	n.d.	n.d.
Oxide	**MZB2-10**	**MZB2-11**	**MZB2-12**	**MZB2-13**	**MZB2-15**	**MZB2-16**	**MZCG-01**	**MZPI-01**	
Na_2O	2.4 (0.4)	3.5 (0.2)	1.8 (0.1)	2.7 (0.1)	2.3 (0.1)	2.5 (0.1)	4.3 (0.1)	2.7 (0.3)	
MgO	5.6 (0.4)	7.0 (0.4)	7.7 (0.2)	4.4 (0.5)	4.6 (0.3)	3.9 (0.5)	3.5 (0.1)	8.4 (0.8)	
Al_2O_3	8.8 (0.3)	7.2 (0.3)	7.2 (0.4)	10.2 (0.2)	8.4 (0.2)	9.0 (0.6)	9.6 (0.2)	4.1 (0.2)	
SiO_2	42.6 (0.6)	42 (2)	40.1 (0.8)	48.1 (0.6)	50.3 (0.8)	51.4 (0.5)	52 (1)	17.4 (0.4)	
SO_3	1.1 (0.2)	1.3 (0.3)	1.1 (0.1)	0.4 (0.3)	0.7 (0.3)	0.8 (0.2)	1.05 (0.08)	2.5 (0.2)	
K_2O	2.5 (0.1)	1.8 (0.2)	1.8 (0.1)	2.5 (0.2)	2.07 (0.02)	2.4 (0.2)	2.0 (0.1)	0.8 (0.1)	
CaO	28.5 (0.3)	29.2 (0.8)	34.4 (0.7)	21.4 (0.4)	24.6 (0.4)	20 (1)	14.2 (0.3)	35 (1)	
TiO_2	n.d.	n.d.	0.2 (0.2)	0.7 (0.2)	0.6 (0.4)	0.4 (0.1)	0.56 (0.09)	0.3 (0.1)	
MnO	n.d.	n.d.	n.d.	n.d.	n.d.	n.d.	0.1 (0.1)	0.3 (0.3)	
FeO	6.1 (0.1)	4.6 (0.3)	4.7 (0.1)	8.2 (0.5)	5.5 (0.2)	8 (1)	9.7 (0.7)	24.4 (0.3)	
CuO	n.d.	n.d.	n.d.	n.d.	n.d.	n.d.	n.d.	1.3 (0.7)	
ZnO	n.d.	n.d.	n.d.	n.d.	n.d.	n.d.	0.2 (0.2)	0.8 (0.9)	
PbO	n.d.	n.d.	n.d.	n.d.	n.d.	n.d.	n.d.	0.3 (0.5)	
BaO	n.d.	n.d.	n.d.	n.d.	n.d.	n.d.	n.d.	0.5 (0.5)	

n.d.: not detected.

The mineralogical composition of the samples was determined by combining FESEM-EDX, XRD, and FTIR. The diffractograms and IR spectra of the sediments around the wreck were dominated by intense quartz and biotite features. Calcite and Mg-calcite were also present. Weak signatures of alkaline feldspars, pyroxene, plagioclase feldspars, hematite, goethite, titanomagnetite, and clayey minerals of the kaolinitic type were also identified (Figures 8 and 9 and Table S6). A reduction in the intensity of hematite and goethite features occurred within the MZB2-01 spectra taken from under the anchor (Figures 8c and 9c). Sediment MZGC-01 from Cabezo del Gavilán showed a higher iron oxide content than the near-wreck samples (Figure 9b). Sediment MZPI-01 from El Gachero had higher Mg-calcite hematite and goethite contents than the near-wreck samples. Wollastonite, magnetite, maghemite, fayalite, and kirchseinite were also identified in this sediment (Figures 8d and 9d, Table S6). The other minerals to be identified at minor/trace levels within the X-ray spectra were halite, titanite, sodium feldspars, sillimanite, cordierite, garnet, zircon, apatite, augite, rutile, ilmenite, titanomagnetite, pyrite, and mackinawite (Table S7).

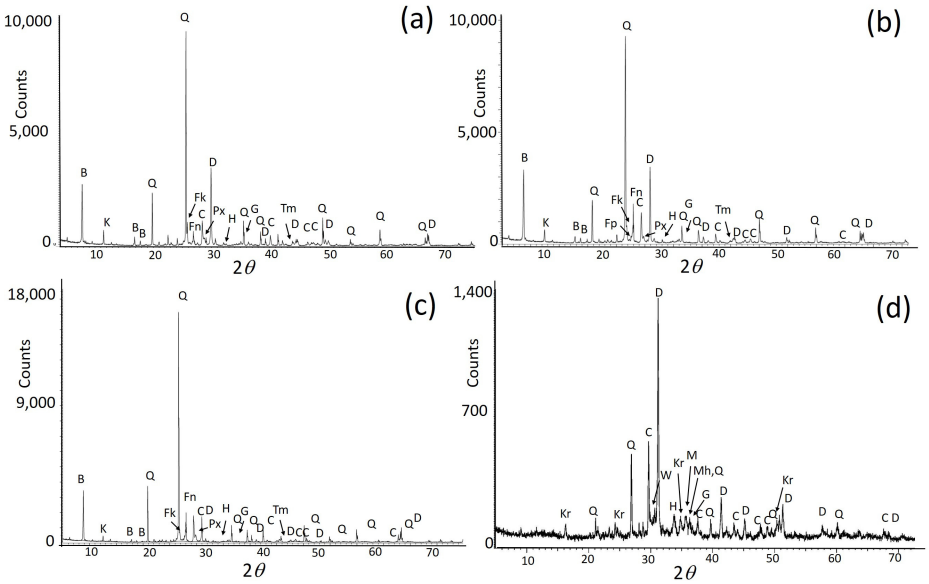

Figure 8. Diffractograms acquired from samples: (**a**) MZB2-11; (**b**) MZB2-02; (**c**) MZB2-01; (**d**) MZPI-01. B: biotite; C: calcite; D: dolomite; G: goethite; H: hematite; K: kaolinitic clayey minerals; M: magnetite; Mh: maghemite; Kr: kirchseinite; Q: quartz; Fk: K-feldspar; Fn: Na-feldspar; Fp: plagioclase feldspar; Px: pyroxene; Tm: titanomagnetite; W: wollastonite.

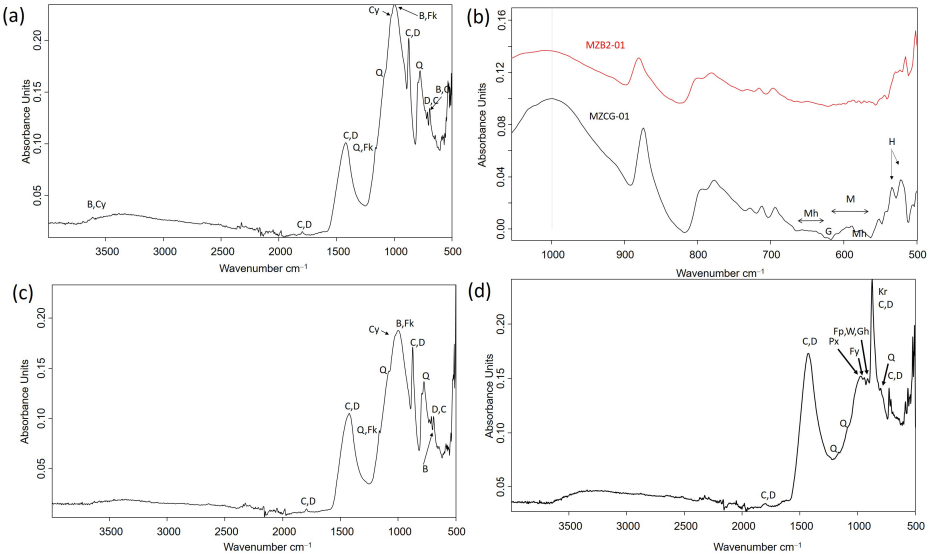

Figure 9. IR absorption spectra acquired from samples: (**a**) MZCG-01; (**b**) detail of MZB2-01 and MZCG-01 within the IR spectra as 500–1000 cm^{-1}; (**c**) MZB2-01 and (**d**) MZPI-01. B: biotite; C: calcite; C_y: clays; D: dolomite; Fk: potassium feldspar; Fp: plagioclase feldspar; Fy: fayalite; G: goethite; Gh: gehlenite; H: hematite; Kr: kirchsteinite; M: magnetite; Mh: mahemite; Px: pyroxene; Q: quartz; W: wollastonite.

4.2.3. Redox Status

The DOP values provided an estimate of the samples' redox status. The average DOP values that were determined in the set of samples are summarized in Table S8. The DOP values reported from samples MZB2-02 to MZB2-16 and MZCG-01 were <0.45 and correspond to an oxic environment. The DOP value reported in sample MZ-01 was 0.66 and corresponds to a dysoxic environment. The highest value, 0.82, reported for sample MZPI-01 from El Gachero corresponded mainly to the pyrite present in slags and to the pyrites formed in the furnace as a consequence of the chemical reaction between soluble ions Fe^{2+} and S^{2-}.

4.3. Wood Samples

The waterlogged wood samples MAZ-01 and MAZ-02 obtained BD values of 0.17 and 0.19 g cm^{-3}, respectively, which confirm the wreck wood's high decay level. Figure 10 displays three projections, which were obtained at different depths while scanning the fragment MAZ-01 cross-section by XRM. The image shows the characteristic anatomical elements of softwood, such as alternated spring and summer growth rings. Mineral aggregates are deposited on the external surface, fill the internal channel of tracheids, and infiltrate along thin fissures that are 0.5 cm long. The content of mineral inclusions drastically drops at ca 0.7 mm inside. Most of them are clusters of pyrite framboids (Figure 11a), but quartz, alkaline feldspars, halite, galena, and mackinawite were also found (Table S7). The IR spectrum acquired from the surface of wood samples exhibits bands at 1560 and 1543 cm^{-1}, assigned to the manganese and calcium carboxylates formed by the complexation of these ions with fatty acids released from wood lipids (Figure S4) [76].

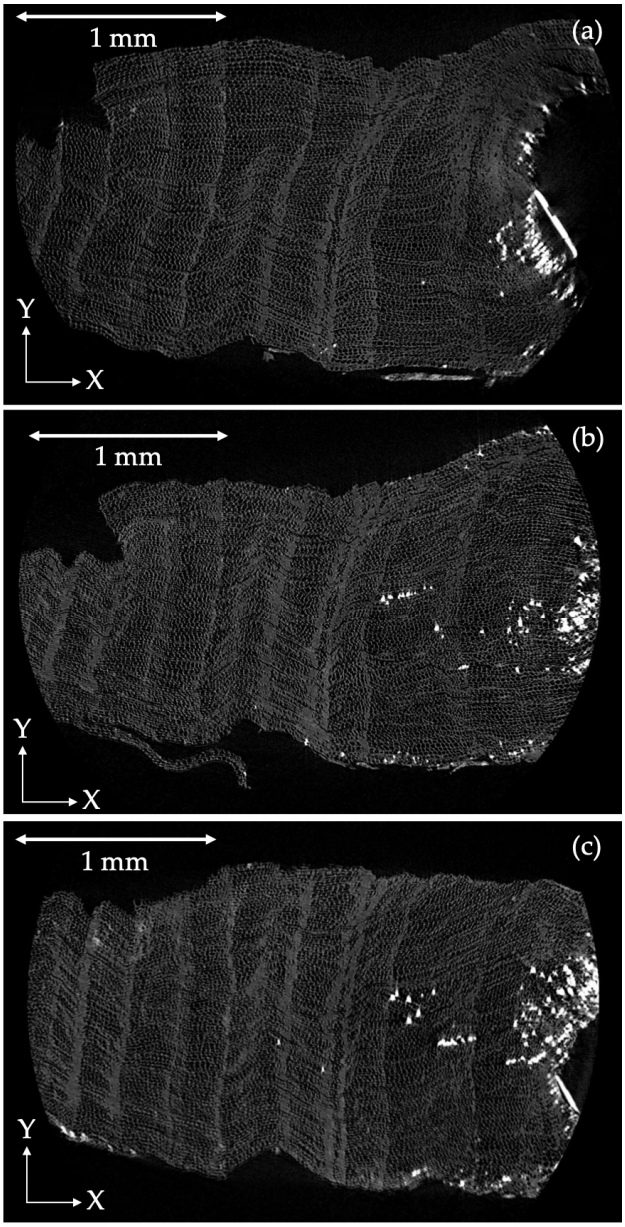

Figure 10. In-depth projections of sample MAZ-01. Coordinates -x and -y in the cross-section plane of the wood, and orthogonal coordinate -z along images (**a**–**c**).

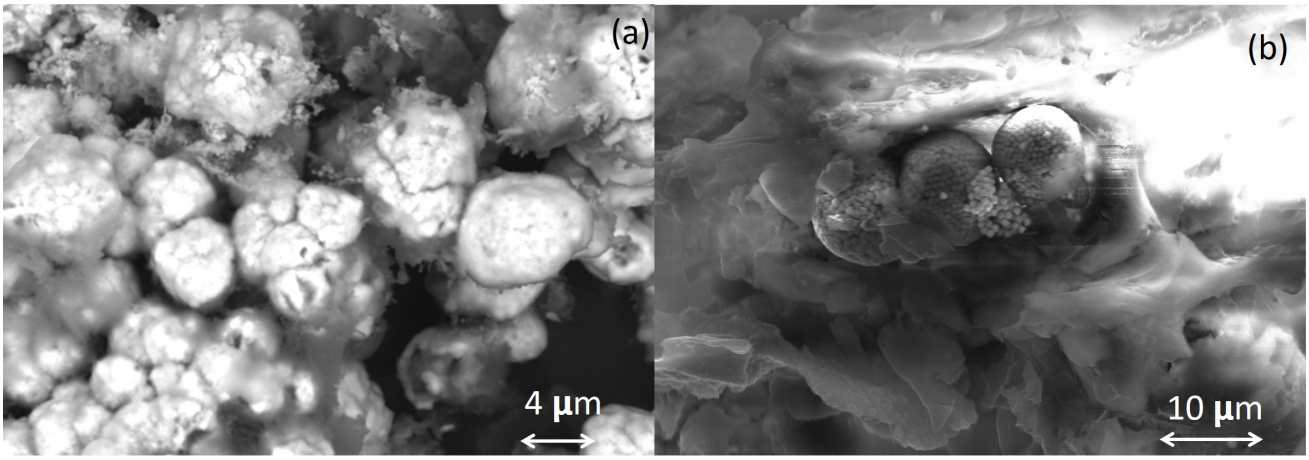

Figure 11. Backscattered electron images (FESEM, 20 kV): (**a**) aggregates and clusters of framboidal pyrites in sample MAZ-01; (**b**) spherulitic aggregates of framboidal pyrite growing in the internal channel of a tracheid in MAZ-02.

5. Discussion

5.1. Sediment Biogeochemistry

The mineralogical composition of the terrigenic part of the sediments was in accordance with the geology of the Mazarrón region. The results obtained from the sediments found in the surroundings of the wreck (MZB2-@ series) and at Cabezo del Gavilán (MZCG-01) suggest that most minerals are derived from the rocks that have shaped the geological region of Mazarrón. According to López Ruíz et al. [77,78], the Mazarrón region is mainly composed of calc-alkaline and potassic volcanogenic rocks that have undergone further metamorphism episodes. Andesitic and dacitic rocks, and those of the shoshonitic type, including banakite and latite, were the most remarkable. Most of the minerals that composed these rocks, such as plagioclase, alkaline feldspars, sillimanite, biotite, cordierite, garnet, and augite, appeared in the analyzed sediments, which confirmed the weathering processes that have led rocks to disaggregate and be transported to the sea. A second source of terrigenic grains of calcite composition is an extensive region that occupies the lowest topographic areas along the shoreline, composed of post-orogenic sedimentary rocks, mostly from the Quaternary age and the rest from the Neogene. It is a marly–sandy detrital series with levels of marls alternating with sandstones and sands, clogged by a Quaternary cover formed by conglomerates of heterometric pebbles and calcareous matrix. The disposition of these materials is subhorizontal.

The FESEM-EDX analysis confirmed that most grains exhibited the typical composition of impure minerals due to the disaggregation of the above rocks [79]. Quartz and feldspar grains had interstitial or substitute ions in the silica lattice [80] (Table S7). Other minerals, which were found as inclusions of quartz grains, were biogenic apatite (A_p) (Figure S5a), pyrite (P_y), iron oxides (I_o), and lead-rich microcrystals (Pb) (Figure S5b).

The biogenic minerals were the remains of planktic and benthic organisms and biogenic apatite. They included silica, calcite, and Mg-calcite. Chemogenic minerals, including pyrite and mackinawite formed in superficial sediments, are considered in the next section.

There was one important part of the El Gachero (MZPI-01) sediments that was composed of the by-product slags formed during the processing of raw minerals in furnaces [81]. These materials consisted mainly of iron oxides that contained other metal impurities (Pb, Zn, Ba, Al, Ca, and Mg), accompanied by kirschsteinite ($CaFeSiO_4$) (K) (Figure S6), titanomagnetite, and titanite. Slag particles were also present in samples MZB2-@ and MZCG-01.

Some correlations were established among the sampling points, chemical composition, color, and PSD. The sediments showed color progression following a south–north profile and in such a way that the samples acquired lighter and pale brown-yellowish hues when one passed from south to north (Figure 12). The PSD also followed a gradation. Silt was

also predominantly found in the sediments from the northern part, while sand prevailed in the near-wreck sediments, and the sediments containing more gravel were found on the periphery of the south site. The chemical composition also exhibited a south–north profile. The calculated mean values for the calcium oxide percentage in the three color areas exhibited an increasing south–north profile, while the iron oxide percentages showed the opposite trend. Therefore, the light brownish silt-rich sediments that occurred in the northern area outside the metallic coffer were associated with significant contents of brownish clayey and grayish calcite. A mixture of silt and fine sand minerals prevailed in the pale yellowish-brown sediments of the area inside the wreck coffer, with significant contents of iron oxides, quartz, and feldspars. In the brownish sandy-gravel sediments from the southern part, the dark iron oxides and the highest black biotite contents, confirmed by XRD, were significantly prevalent.

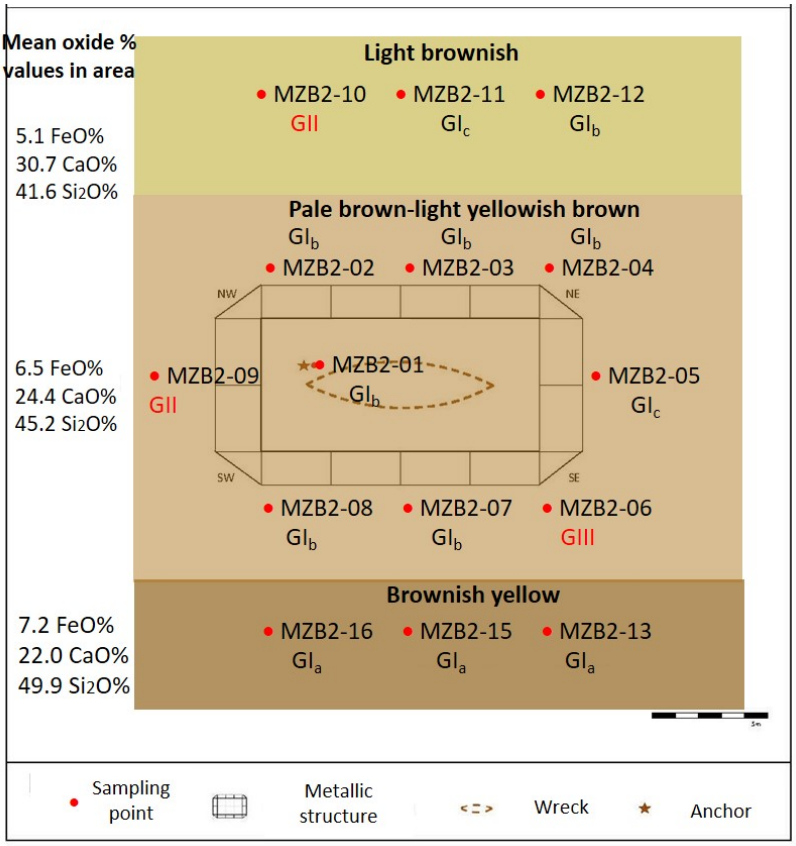

Figure 12. Correlations among sampling points MZB2-01 to MZB2-16, color, particle size distribution types GI_a, GI_b, GI_c, GII and GIII, and silica, iron and calcium oxide content of sediments.

These results could be tentatively related to the changed marine coastal dynamics, which have influenced the water circulation around the wreck [56]. Hence, the silt composed of clayey and ochre iron oxides and oxyhydroxides in the northern area prevailed because of better sediment transport and oxygen-rich water renovation due to the coastal dynamics. The poor water renovation in the southern part favored the accumulation of dark, larger, and heavier materials, such as biotite or magnetite. The difference between the fine sand sediments at the shipwreck site (MZB2-@) and the medium-sized sand on Playa Bahía (MZCG-01) was also associated with the shallower bathymetric depth on Playa Bahía (−1 m) than at the shipwreck site (−2 m) [82]. A second factor for the lower particle size of the shipwreck sediments was the increased erosion of the central area of Playa de la Isla, promoted by the nearby marina being built.

5.2. Chemical Processes in Sediments

The main processes that can affect the wreck's integrity, associated with sediments and their biogeochemistry, lay in the iron cycle that involves precipitation, dissolution, and redox processes (Figure S7). In either the upper sediments or the euxinic water column, hydrogen sulfide and Fe^{2+} can nucleate to form monosulfide precursors, which lead to pyrite precipitation [83]. The iron oxides, oxyhydroxides, magnetite, and clays present in sediments in the solid state are dissolved to Fe^{2+} via reductive dissolution under anoxic or suboxic conditions. Iron reduction may also occur through dissimilatory reducing microorganisms, which couple this process with organic carbon or S^{2-} oxidation [84,85]. Sulfate-reducing bacteria reduce SO_4^{2-} to H_2S. These processes lead to a higher Fe^{2+} content, which favors the formation of iron sulfide species [83]. Mechanisms of pyrite precipitation, intermediated by related iron sulfides, have been proposed and are based on the oxidation of iron sulfides by H_2S or polysulfides [86,87]. Nevertheless, part of the dissolved Fe^{2+} can diffuse upwardly and undergo oxidation with oxygen, nitrate, or manganese oxides. Fe^{3+} can accumulate on the redoxcline to form iron oxides and lead to an iron-rich layer immediately above. This redoxcline or redox boundary is defined roughly by the oxygen penetration depth and DOP [84]. Then, formed oxides can diffuse downward below the redox boundary to complete the active cycle of the iron displacement around the redox boundary [2].

Skeletons and shells of diatoms, foraminifera, and other benthonic species provide microenvironments in which the exchange of ionic species is restricted. Here, iron sulfide process precipitation is promoted by the easy oxidation undergone by the organic matter of the soft parts mediated by microorganisms. Simultaneously, electronic receptors, such as Fe^{3+} and SO_4^{2-} (but also O_2 and Mn^{4+}), are reduced (e.g., Fe^{3+} is reduced to Fe^{2+}; SO_4^{2-} is reduced to S^{2-}) [83].

Chemogenic pyrite can adopt different morphologies as follows: single crystals (cube, octahedron, and pyritohedron; diameter of <2 μm) and their aggregates, particularly the spherulitic aggregates termed framboids (diameter, 4–50 μm) and framboids clusters. Several studies carried out in recent decades have demonstrated that these pyrite structures can be used for establishing the type of redox status of the depositional environment in which they have been formed as an alternative method to determine the DOP values [83,88–91]. In this study, a correlation was established between the DOP values and the pyrite features identified in the sediments. Three different sample groups can be discriminated according to the DOP, pyrite crystals, and aggregates morphology.

The first sample group included the near-wreck MZB2-@ and MZGC-01 samples, which were taken at depths ranging from 20 cm to 30 cm. The DOP values reported for these sediments were < 0.45, which corresponds to an oxic environment. This result agreed with the almost total lack of pyrite formations, which were limited to isolated features in biogenic grains (Figure 13a,b). The diameters of the framboidal aggregates that formed were <10 μm, which corresponds to a dysoxic environment. The reductive status inside the porous patterns of biogenic grains favored pyrite precipitation, as previously described.

The second group of sediments included sample MZB2-01, taken at a depth of 80 cm below the anchor. Many framboidal aggregates and small clusters were found in the microcavities of biogenic grains and sometimes in mineral grains (Figure 13c). The DOP value of 0.66, reported for this sediment, corresponds to a dysoxic environment in accordance with the profusion and complexity of the pyrite formations found in this deeper sediment.

The third group included sample MZPI-01 (El Gachero). The DOP value (0.82) for this sample corresponds to an anoxic environment (DOP > 0.7). The sample was characterized by the presence of individual pyrite framboids, which had sometimes formed close to sources of Fe^{3+} ions, such as iron oxide grains of by-product slags or biogenic grains (Figure 13d). Such abundance and morphology are more characteristic of dysoxic environments. This apparent discrepancy between morphology and the DOP can be justified by the large amount of non-authigenic pyrite and the related compounds contained in the by-product slags that contribute to an increase in the DOP value.

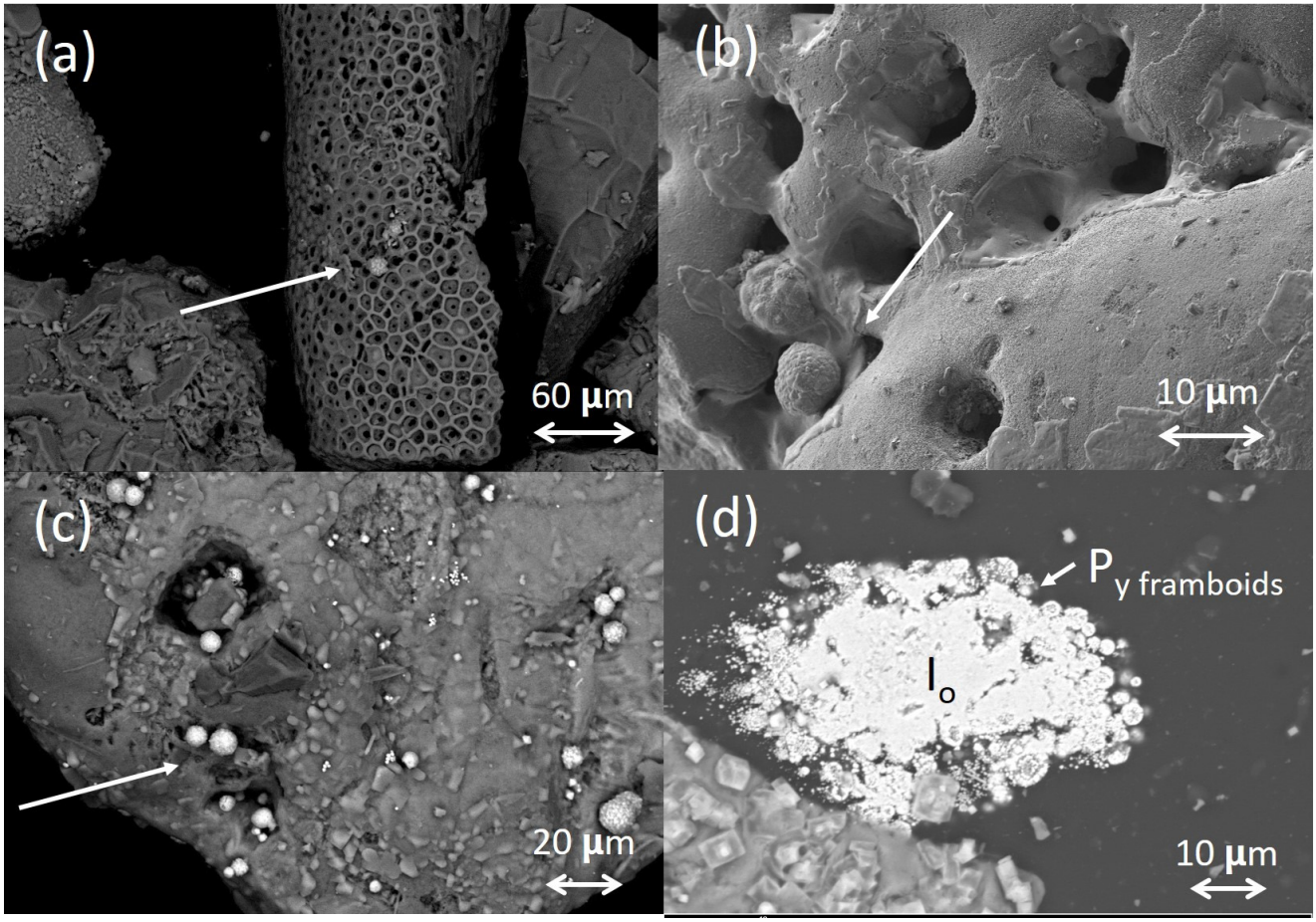

Figure 13. Backscattered electron image (20 kV) (**a**,**c**,**d**) and the secondary electron image (2 kV) (**b**) of the framboidal pyrites identified in (**a**) sample MZB2-05); (**b**) sample MZB2-08; (**c**) sample MZB2-01 below the anchor; (**d**) sample MZPI-01 from El Gachero.

5.3. Chemical Processes in Wood

As described above, the fissures and internal channels of the tracheids in the wood samples contained plenty of clusters of framboidal pyrite. The framboids exhibited broad-sized distributions with values of up to 10 µm. This suggests that the internally degraded wood structure shaped a dysoxic–anoxic microenvironment, which promotes pyrite formation. This microenvironment not only promotes redox processes like the reduction of Fe^{3+} or SO_4^{2-}, but also other reactions that require a certain concentration of metal ions. The identification of metal carboxylate complexes by FTIR spectroscopy (Figure S4) denoted that, inside channels, metal ions like Ca^{2+} or Mn^{2+} accumulated and were prone to react via complexation.

The analyses for determining the lead concentration in the samples from the water column and sediments were conducted to assess the possible effect of the lead cargo transported by the ship as pollution sources (data not reported). No significant differences were found in the results obtained in the three studied areas, namely, El Gachero, the shipwreck site, and Cabezo del Gavilán. In all cases, the analytical values were in the order of the background levels established for the Mediterranean Sea [92,93]. These results suggest that the possible pollutant effect of the lead cargo while it remained in the shipwreck has progressively gone into remission after the cargo was recovered in 2000.

6. Conclusions

The sediments' composition and their biogeochemistry were studied in an attempt to determine their influence on Mazarrón 2's decay. This study demonstrated that the sedi-

ment composition was related to the geological context of the Mazarrón region. Sediments exhibited a similar composition, characterized by a high quartz content and by moderate calcite, Mg-calcite, biotite, and feldspar contents, with abundant impurities and a small amount of other minerals directly related to the rocks in the region.

The influence of the changes in coastal dynamics as a consequence of building a nearby marina in the 20th century caused the gradation in the properties and composition of the sediments surrounding the wreck. These changes also promoted the displacement of the by-product slags from El Gachero to where the wreck is located and slightly modified the sediments' composition. The main minerals associated with the by-product slags were iron oxides, kirschsteinite, and, to a lesser extent, ilmenite, titanite, and titanomagnetite.

This study demonstrated that using the formed pyrite morphology can be a suitable proxy for the sediments' redox status, and the results obtained with the Mazarrón 2 samples agreed with the DOP values.

It also revealed that the iron reductive cycle in superficial sediments notably impacted the wreck's conservation state. In the sediments, pyrite formation occurred prevalently in the dysoxic to anoxic environment inside biogenic grains. Similarly, pores, fissures, and internal channels of wood were from dysoxic–anoxic environments that have favored the formation of large aggregates of pyrite framboids and clusters.

Finally, this study has proven essential for deciding about the raising and conservation treatments for Mazarrón 2. The geotechnical measurements taken demonstrated that the depth of the rock bed beneath the shipwreck area exceeds 1.2 m, which indicates that the raising of the wreck can proceed in block or without significant fragmentation [37], contrary to another proposal of extraction on portions [38].

Supplementary Materials: The following Supporting material can be downloaded at: https://www.mdpi.com/article/10.3390/min14080778/s1, Tables S1–S8; Figures S1–S7. Table S1. List of samples and main characteristics. Table S2. Instruments and operating conditions. Table S3. Depth values obtained with the Jacob's Staff inside the wreck and outside the metallic protection structure. Table S4. The Hue Value and Chroma of sediments determined by Munsell soil colour chart for the samples. Table S5. Summary of particle size distribution (PSD) analysis: grain size percentage (% of gravels, % of sands, and % of fines); D10, D30 and D60 are the particle sizes corresponding to 10, 30, and 60% finer on the cumulative particle size distribution curve, respectively; coefficient of uniformity (Cu) and curvature (Cc), and sedimentary textures description (group symbol, USCS). SP: Poorly graded sand with gravel; SP SM: Poorly graded sand with silt and gravel; GP GM: Poorly graded gravel with silt and sand; SM: Silty sand with gravel; SP SM: Poorly graded sand with silt and gravel; SM: Silty sand with gravel; GM: Silty gravel with sand. Table S6. IR absorption bands from the IR spectra acquired in sediment samples and wreck wood samples. Table S7. Experimental chemistry obtained from the sediment grains of the samples prepared as cross-section and from the wood samples analyzed by FESEM-EDX. Table S8. Average DOP values determined in the set of samples analyzed. Relative standard deviations values are in the range 5–45%. Figure S1. Backscattered electron images acquired in samples of sediments prepared as cross-section at 20kV: (a) MZB2-07; (b) MZPI-01. Ap: apatite; B: biotite; B_x: biotite inclusions; C: calcite; D: dolomite; F_{Na}: sodium feldspar; F_K: potassium feldspar; Io: iron oxide; I_{Mn}: iron oxide with manganese traces; I_{Zn}: iron oxide with zinc traces; Q: quartz; T_m: titanomagnetite; Ti: titanite. Figure S2. Particle Size Distribution curves for Groups I_a to I_c; Figure S3: Particle Size Distribution curves for Groups II to IV; Figure S4: IR absorption spectrum acquired in sample MAZ-01. The arrow points the narrow region of IR bands from metal-carboxylate complexes. Figure S5: Backscattered electron image (20 kV) of the cross-section of: (a) a grain of quartz with biogenic apatite inclusion in sample MZB2-10; (b) a grain of quartz with iron oxide, pyrite and lead-rich mineral inclusions in sample MZB2-4. Q: quartz; Ap: biogenic apatite; Py: pyrite; Pb: lead-rich mineral. Figure S6: Backscattered electron image (20 kV) of the cross-section of a grain of slag. Figure S7: Scheme of the iron reductive cycle in surficial sediments.

Author Contributions: Conceptualization, M.-T.D.-C.; methodology, M.-T.D.-C. and N.G.-F.; software, C.Á.-R.; formal analysis, M.-T.D.-C.; investigation, M.-T.D.-C., N.G.-F., C.Á.-R., M.B.-O., S.P.-M. and R.C.-B.; resources, M.-T.D.-C., M.B.-O., S.P.-M. and R.C.-B.; data curation, M.-T.D.-C., M.B.-O., S.P.-M. and R.C.-B.; writing—original draft preparation, M.-T.D.-C., N.G.-F., C.Á.-R., M.B.-O., S.P.-M. and

R.C.-B.; writing—review and editing, M.-T.D.-C., N.G.-F., C.Á.-R., M.B.-O., S.P.-M. and R.C.-B.; visualization, M.-T.D.-C., N.G.-F., C.Á.-R., M.B.-O., S.P.-M. and R.C.-B.; supervision, M.-T.D.-C.; project administration, M.-T.D.-C., M.B.-O., S.P.-M. and R.C.-B.; funding acquisition, M.-T.D.-C., M.B.-O., S.P.-M. and R.C.-B. All authors have read and agreed to the published version of the manuscript.

Funding: This research was funded by MCIN/AEI/10.13039/501100011033, Fondo Europeo de Desarrollo Regional (ERDF), and Agencia Estatal de Investigación (AEI), grant PID2020-113022GB-I00. It also obtained a Margarita Salas grant from the Requalification program of the Spanish University System of the Ministry of Universities, financed by the European Union-NextGenerationEU.

Data Availability Statement: Data are contained within this article and Supplementary Materials.

Acknowledgments: We acknowledge the technical support of Manuel Planes-Insausti, José Luis Moya-López, Alicia Nuez-Inbernón, Mercedes Tabernero-Mendoza, and Joaquín Fayos-Febrer, technical supervisors of the Servicio de Microscopía, of the Universitat Politècnica de València.

Conflicts of Interest: The authors declare no conflicts of interest. The funders had no role in the design of the study, in the collection, analyses, or interpretation of data, in the writing of the manuscript, or in the decision to publish the results.

References

1. Gregory, D.; Jensen, P.; Strætkvern, K. Conservation and in situ preservation of wooden shipwrecks from marine environments. *J. Cult. Herit.* **2012**, *13*, S139–S148. [CrossRef]
2. Burdige, D.J. *Geochemistry of Marine Sediments*; Princeton University Press: Princeton, NJ, USA, 2006.
3. Lehtoranta, J.; Petri Ekholm, P.; Pitkänen, H. Coastal Eutrophication Thresholds: A Matter of Sediment Microbial Processes. *AMBIO J. Hum. Environ.* **2009**, *38*, 303–308. [CrossRef] [PubMed]
4. Kuznetsova, O.V.; Sevastyanov, V.S.; Timerbaev, A.R. What are the current analytical approaches for sediment analysis related to the study of diagenesis? Highlights from 2010 to 2018. *Talanta* **2019**, *191*, 435–442. [CrossRef] [PubMed]
5. Nigam, R. Geological/paleontological applications in marine archeology: Few examples from Indian waters. In *The Role of Tropics in Climate Change*; Khare, N., Ed.; Elsevier: Amsterdam, The Netherlands, 2024; pp. 419–439.
6. Romano, E.; Magno, M.C.; Bergamin, L. Grain Size Data Analysis of Marine Sediments, From Sampling to Measuring and Classifying. A Critical Review. In Proceedings of the IMEKO International Conference on Metrology for The Sea, Naples, Italy, 11–13 October 2017.
7. Jensen, P.; Gregory, D.J. Selected physical parameters to characterize the state of preservation of waterlogged archaeological wood: A practical guide for their determination. *J. Archaeol. Sci.* **2006**, *33*, 551–559. [CrossRef]
8. Łucejko, J.J.; Modugno, F.; Ribechini, E.; del Río, J.C. Characterisation of archaeological waterlogged wood by pyrolytic and mass spectrometric techniques. *Anal. Chim. Acta* **2009**, *654*, 26–34. [CrossRef] [PubMed]
9. Pizzo, B.; Giachi, G.; Fiorentino, L. Reasoned use of chemical parameters for the diagnostic evaluation of the state of preservation of waterlogged archaeological wood. *J. Archaeol. Sci.* **2013**, *40*, 1673–1680. [CrossRef]
10. Macchioni, N.; Pizzo, B.; Capretti, C.H.; Giachi, G. How an integrated diagnostic approach can help in a correct evaluation of the state of preservation of waterlogged archaeological wooden artefacts. *J. Archaeol. Sci.* **2012**, *39*, 3255–3263. [CrossRef]
11. Łucejko, J.J.; Modugno, F.; Ribechini, E.; Tamburinia, D.; Colombini, M.P. Analytical Instrumental Techniques to Study Archaeological Wood Degradation. *Appl. Spectrosc. Rev.* **2015**, *50*, 584–625. [CrossRef]
12. Babinski, L.; Izdebska-Mucha, D.; Waliszewska, B. Evaluation of the state of preservation of waterlogged archaeological wood based on its physical properties: Basic density vs. wood substance density. *J. Archeol. Sci.* **2014**, *46*, 372–383. [CrossRef]
13. Čufar, K.; Gričar, J.; Zupančič, M.; Koch, G.; Schmitt, U. Anatomy, cell wall structure and topochemistry of water-logged archaeological wood aged 5200 and 4500 years. *IAWA J.* **2008**, *29*, 55–68. [CrossRef]
14. Björdal, C.G.; Nilsson, T.; Daniel, G. Microbial decay of waterlogged archaeological wood found in Sweden. Applicable to archaeology and conservation. *Int. Biodeterior. Biodegrad.* **1999**, *43*, 63–73. [CrossRef]
15. Christensen, M.; Frosch, M.; Jensen, P.; Schnell, U.; Shashoua, Y.; Nielsen, O.F. Waterlogged archaeological wood—Chemical changes by conservation and degradation. *J. Raman Spectrosc.* **2006**, *37*, 1171–1178. [CrossRef]
16. Li, R.; Guo, J.; Macchioni, N.; Pizzo, B.; Xi, G.; Tian, X.; Chen, J.; Sun, J.; Jiang, X.; Cao, J.; et al. Characterisation of waterlogged archaeological wood from Nanhai No. 1 shipwreck by multidisciplinary diagnostic methods. *J. Cult. Herit.* **2022**, *56*, 25–35. [CrossRef]
17. Traoré, M.; Kaal, J.; Martínez Cortizas, A. Chemometric tools for identification of wood from different oak species and their potential for provenancing of Iberian shipwrecks (16th–18th centuries AD). *J. Archeol. Sci.* **2018**, *100*, 372–383. [CrossRef]
18. Giachi, G.; Bettazzi, F.; Chimichi, S.; Staccioli, G. Chemical characterisation of degraded wood in ships discovered in a recent excavation of the Etruscan and Roman harbour of Pisa. *J. Cult. Herit.* **2004**, *4*, 75–83. [CrossRef]
19. Shen, D.; Li, N.; Fu, Y.; Macchioni, N.; Sozzi, L.; Tian, X.; Liu, J. Study on wood preservation state of Chinese ancient shipwreck Huaguangjiao I. *J. Cult. Herit.* **2018**, *32*, 53–59. [CrossRef]

20. Zoia, L.; Salanti, A.; Orlandi, M. Chemical characterization of archaeological wood: Softwood Vasa and hardwood Riksapplet case studies. *J. Cult. Herit.* **2015**, *16*, 428–437. [CrossRef]
21. MacLeod, I.D. Conservation of waterlogged timbers from the Batavia 1629. *Bull. Aust. Marit. Archeol.* **1990**, *14*, 1–8.
22. Zhang, H.; Shen, D.; Zhang, Z.; Kang, H.; Ma, Q. Comparison of iron deposits removing material from the marine archaeological wood of Nanhai I shipwreck. *J. Cult. Herit.* **2024**, *66*, 59–67, and references therein. [CrossRef]
23. Bjurhager, I.; Halonen, H.; Lindfors, E.L.; Iversen, T.; Almkvist, G.; Gamstedt, E.K.; Berglund, L.A. State of degradation in archeological oak from the 17th century Vasa ship: Substantial strength loss correlates with reduction in (holo)cellulose molecular weight. *Biomacromolecules* **2012**, *13*, 2521–2527. [CrossRef]
24. Fors, Y.; Jalilehvand, F.; Risberg, E.D.; Björdal, C.; Phillips, E.; Sandström, M. Sulfur and iron analyses of marine archaeological wood in shipwrecks from the Baltic Sea and Scandinavian waters. *J. Archeol. Sci.* **2012**, *39*, 2521–2532. [CrossRef]
25. Smith, A.D.; Jones, M.; Berko, A.; Chadwick, A.V.; Newport, R.J.; Skinner, T.; Salomé, M.; Fredrick, J.; Mosselmans, W. An investigation of the Sulfur–Iron chemistry in timbers of the sixteenth century warship, the Mary Rose, by Synchrotron micro-X-ray spectroscopy. In Proceedings of the 37th International Symposium on Archaeometry, Siena, Italy, 13–16 May 2008; pp. 389–394.
26. North, N.A.; MacLeod, I.D. Corrosion of metals. In *Conservation of Marine Archaeological Objects*; Pearson, C., Ed.; Butterworth-Heinemann: Amsterdam, The Netherlands, 1987.
27. Almkvist, G.; Persson, I. Distribution of iron and sulfur and their speciation in relation to degradation processes in wood from the Swedish warship Vasa. *New. J. Chem.* **2011**, *35*, 1491–1502. [CrossRef]
28. Sandström, M.; Jalilehvand, F.; Damian, E.; Fors, Y.; Gelius, U.; Jones, M.; Murielle, S. Sulfur accumulation in the timbers of King Henry VIII's warship Mary Rose: A pathway in the sulfur cycle of conservation concern. *Proceedings of the National Academy of Sciences* **2005**, *102*, 14165–14170. [CrossRef] [PubMed]
29. Bettazzi. F.; Giachi, G.; Staccioli, G.; Chimichi, S. Chemical characterisation of wood of Roman Ships brought to light in the recently discovered ancient Harbour of Pisa (Tuscany, Italy). *Holzforschung* **2003**, *57*, 373–376. [CrossRef]
30. Rémazeilles, C.; Tran, K.; Guilminot, E.; Conforto, E.; Refait, P. Study of iron (II) sulphides by environmental scanning electron microscopy (ESEM) and micro-Raman spectroscopy in waterlogged archaeological woods. In Proceedings of the International Conference on Non-Destructive Investigations & Microanalysis for the Diagnostics & Conservation of Cultural & Environmental Heritage, Florence, Italy, 13–15 April 2011; pp. 297–307.
31. Rémazeilles, C.; Meunier, L.; Lévêque, F.; Plasson, N.; Conforto, E.; Crouzet, M.; Refalt, P.; Caillat, L. Posttreatment study of Iron/Sulfur-containing compounds in the wreck of Lyon Saint-Georges 4 (Second Century ACE). *Stud. Conserv.* **2019**, *65*, 28–36. [CrossRef]
32. Zhang, Z.G.; Li, N.S.; Tian, X.L.; Liu, J.; Shen, D.W. Research on the removal of the iron sulfides in the Qing Dynasty marine shipwreck, Ningbo Xiaobaijiao No. 1. *Sci. Conserv. Archaeol.* **2014**, *26*, 30–38.
33. Vieira, H.C.; Bordalo, M.D.; Osten, J.R.V.; Soares, A.M.; Abreu, S.N.; Morgado, F. Can a 16th Century Shipwreck Be Considered a Mercury Source in the 21st Century?—A Case Study in the Azores Archipelago (Portugal). *J. Mar. Sci. Eng.* **2023**, *11*, 276. [CrossRef]
34. Negueruela, I.; Pinedo, J.; Gómez, M.; Miñano, A.; Arellano, I.; Barba, J.S. Seventh-century BC Phoenician vessel discovered at Playa de la Isla, Mazarron, Spain. *Int. J. Naut. Archaeol.* **1995**, *24*, 189–197. [CrossRef]
35. Negueruela, I. Protection of shipwrecks: The experience of the Spanish National Maritime Archaeological Museum. In *Underwater Archaeology and Coastal Management. Focus on Alexandria*; Hassan, M., Grimal, N., Nakashima, D., Eds.; UNESCO: París, France, 2000; pp. 111–116.
36. Negueruela, I. The Phoenician Ships of Mazarrón. In *Assyria to Iberia at the Dawn of the Classical Age*; Aruz, J., Graff, S.B., Rakic, Y., Eds.; The Metropolitan Museum of Art: New York, NY, USA, 2014; pp. 243–245.
37. Castillo, R.; Pérez, S.; Buendía, M. Una historiografía del pecio Mazarrón 2. In *Actas de la Reunión Internacional de Expertos Sobre la Extracción y Conservación del Pecio Mazarrón 2*; Ministerio de Cultura: Madrid, Spain, 2023; pp. 29–99.
38. de Juan, C. El pecio de Mazarrón 2 (Murcia) y la arquitectura naval venida del Levante. In *Actas de la Reunión Internacional de Expertos Sobre la Extracción y Conservación del Pecio Mazarrón 2*; Ministerio de Cultura: Madrid, Spain, 2023; pp. 15–28.
39. Doménech, T. Analytical techniques and sampling strategies for establishing the state of conservation of underwater archaeological objects. In *Actas de la Reunión Internacional de Expertos Sobre la Extracción y Conservación del Pecio Mazarrón 2*; Ministerio de Cultura: Madrid, Spain, 2023; pp. 271–278.
40. Negueruela, I. Hacia la comprensión de la construcción naval fenicia según el barco "Mazarrón-2" del siglo VII a. C. In *La Navegación Fenicia. Tecnología Naval y Derroteros. Encuentro Entre Marinos, Arqueólogos e Historiadores*; Centro de Estudios Fenicios y Púnicos, Universidad Complutense de Madrid: Madrid, Spain, 2004; pp. 227–278.
41. Gianfrotta, P.A. Le "ancore d'argento" dei mercanti fenici (Diod. V 35, 4): Espediente di carico e precauzione daziaria. *Quad. Aristonothos. Riv. Studi Sul. Mediterr. Antico.* **2021**, *17*, 253–275.
42. Pomey, P. Le dossier de l'épave du Golo (Mariana, Haute-corse). *Archaeonautica* **2012**, *17*, 11–30. [CrossRef]
43. de Juan, C. Los pecios de Mazarrón y la familia arquitectónica ibérica. Los ejemplos más antiguos de la arquitectura naval indígena en la Península Ibérica. In *Mazarrón II. Contexto Arqueológico, Viabilidad Científica y Perspectiva Patri–monial del Barco B-2 De La Bahía de Mazarrón (Murcia). En Homenaje a Julio Mas García*; Universidad Autónoma de Madrid: Madrid, Spain, 2017; pp. 229–254.

44. Ramón, J. Eivissa Fenícia I Les Comunitats Indígenas Del Sud-Est. Contactes: Indígenes i fenicis a la Mediterrània occidental entre els sigles VIII y VI ane. In *Simposi d'Arqueologia d'Alcanar, 24–26 November 2006*; Signes, Disseny i Comunicación: Barcelona, Spain, 2008; pp. 39–53.
45. Ramón, J. La cerámica fenicia del Mediterráneo extremo-occidental y del Atlántico (s. VIII-1r. 1/3 del VI a. C.). Problemas y perspectivas actuales. In *Motya and the Phoenician Ceramic Repertoire between the Levant and the West 9–6th Century BC: Proceedings of the International Conference Held in Rome, 26 February 2010*; Nigro, L., Ed.; pp. 211–253.
46. Miñano, A.I. El Barco 2 de Mazarrón. 2014. Available online: https://www.cultura.gob.es/fragatamercedes/dam/jcr:8af3ffff-0e26-426f-8d34-d4e5b2d273cc/barco-mazarron-2.pdf (accessed on 13 May 2024).
47. Agüera, S.; Iniesta, A.; Martínez, M. El coto minero de San Cristóbal y Los Perules (Mazarrón). Patrimonio Histórico Arqueológico e Industrial. In *Memorias de Arqueología de la Región de Murcia 8*; Editora Regional de Murcia: Murcia, Spain, 1999; pp. 523–550.
48. Ramallo, S.; Arana, R. La minería romana en Mazarrón (Murcia). Aspectos arqueológicos y geológicos. *An. Prehist. Arqueol.* **1985**, *1*, 49–68.
49. Guillén, M.C. Las minas de Mazarrón: El paradigma de un paisaje cultural. Entre la desidia de las administraciones públicas y el absentismo de la población. *Rev. Murc. Antropol.* **2018**, *25*, 95–114.
50. Ros, M.M. Nuevos datos en torno a la presencia fenicia en la Bahía de Mazarrón (Sureste Ibérico). In *El Oriente de Occidente. Fenicios y Púnicos en el Área Ibérica*; Prados, F., Sala, F., Eds.; Servicio de Publicaciones de la Universidad de Alicante: Alicante, Spain, 2017; pp. 79–104.
51. Arellano, I.; Barba, J.S.; Gómez, M.; Miñano, A.I.; Negueruela, I.; Pinedo, J. Proyecto Nave Fenicia: 2ª campaña. In *Memorias de Arqueología de la Región de Murcia 9*; Editora Regional de Murcia: Murcia, Spain, 1999; pp. 219–222.
52. Renzi, M.; Montero, I.; Bode, M. Non-ferrous metallurgy from the Phoenician site of La Fonteta (Alicante, Spain): A study of provenance. *J. Archaeol. Sci.* **2009**, *36*, 2584–2596. [CrossRef]
53. Egea, P.M. Una perspectiva social de la minería contemporánea en Mazarrón. In *Phicaria. III Encuentros Internacionales del Mediterráneo. Minería y Metalurgia en el Mediterráneo y su Periferia Oceánica*; Universidad Popular de Mazarrón: Mazarrón, Spain, 2015; pp. 209–228.
54. Guillén, M.C. *Mazarrón 1900*, 2nd ed.; Ayuntamiento de Mazarrón: Mazarrón, Spain, 2022.
55. Dabrio, C.J. Playas. In *Sedimentología: Del Proceso Físico a la Cuenca Sedimentaria*; Arche, A., Ed.; CSIC: Madrid, Spain, 2010; pp. 441–501.
56. Dabrio, C.J.; Polo, M.D. Dinámica litoral y evolución costera del puerto de Mazarrón (Murcia). *Bol. R. Soc. Esp. Hist. Nat.* **1981**, *79*, 225–234.
57. Munsell. *Munsell Soil Color Charts*; Munsell: Boston, MA, USA, 2009.
58. Hema, B.; Jagadeeswaran, R. A comparative study on soil colour determination through munsell colour chart and hyper spectral remote sensing technique. *Int. J. Chem. Stud.* **2018**, *6*, 2420–2429.
59. *UNE-EN ISO 17892-4:2019*; Investigación y Ensayos Geotécnicos. Ensayos de Laboratorio De Suelos. Parte 4. Determinación de la Distribución Granulométrica. (ISO 17892-4:2016). Asociación Española de Normalización: Madrid, Spain, 2019.
60. *D6913-04*; Standard Test Methods for Particle-Size Distribution (Gradation) of Soils Using Sieve Analysis. ASTM: West Conshohocken, PA, USA, 2009.
61. Seibold, E.; Berger, W.H. Sources and Composition of Marine Sediments. In *The Sea Floor*; Springer: Berlin/Heidelberg, Germany, 1996; pp. 69–95.
62. *D 2487-83*; Classification of Soils for Engineerring Purposes: Annual Book os ASTM Standards. American Society for Testing and Materials: West Conshohocken, PA, USA, 1985.
63. Folk, R.L.; Ward, W.C. Brazos river bar: A study in the significance of grain size parameters. *J. Sed. Petr.* **1957**, *27*, 3–26. [CrossRef]
64. Royse, C. *Introduction To Sedimentary Analysis*; Arizona State University Publications: Tempe, AZ, USA, 1970.
65. *D2487-17e1*; Standard Practice for Classification of Soils for Engineering Purposes (Unified Soil Classification System). ASTM International: West Conshohocken, PA, USA, 2017.
66. Berner, R. Sedimentary pyrite formation. *Am. J. Sci.* **1970**, *268*, 1–23. [CrossRef]
67. Álvarez-Iglesias, P.; Rubio, B. Early diagenesis of organic-matter-rich sediments in a ría environment: Organic matter sources, pyrites morphology and limitation of pyritization at depth. *Estuar. Coast. Shelf Sci.* **2012**, *100*, 113–123. [CrossRef]
68. Leventhal, J.; Taylor, C. Comparison of methods to determine degree of pyritization. *Geochim. Cosmochim. Acta* **1990**, *54*, 2621–2625. [CrossRef]
69. Huerta-Diaz, M.A.; Morse, J.W. Quantitative Method for Determination of Trace Metal Concentrations in Sedimentary Pyrite. *Mar. Chem.* **1990**, *29*, 119–144. [CrossRef]
70. Erdey, L.; Bodor, E. Ascorbic Acid in Analytical Chemistry. Determination of Ferric Irons. *Anal. Chem.* **1952**, *24*, 418–420. [CrossRef]
71. Metodiev, L.; Georgieva, M.; Stoylkova, T. Degree of Pyritization (DOP) and Indicator of Anoxicity (IA) in Jurassic sedimentary rocks from Bulgaria. *Rev. Bulg. Geol. Soc.* **2022**, *83*, 149–152. [CrossRef]
72. Raiswell, R.; Newton, R.; Wignall, P.B. An indicator of water-column anoxia: Resolution of biofacies variations in the Kimmeridge clay (upper Jurassic, U.K.). *J. Sediment. Res.* **2001**, *71*, 286–294.

73. Silva, P.G.; Roquero, E.; Rodríguez-Pascua, M.A.; Bardají, T.; Huerta, P.; Giner, J.L.; Pérez-López, R. Development of a numerical system and field-survey charts for earthquake environmental effects based on the Munsell Soil Color Charts. INQUA Focus Group on Paleoseismology and Active Tectonics. In Proceedings of the 4th International INQUA Meeting on Paleoseismology, Active Tectonics and Archeoseismology (PATA), Aachen, Germany, 9–14 October 2013.
74. Wentworth, C.K. A Scale of Grade and Class Terms for Clastic Sediments. *J. Geol.* **1922**, *30*, 377–392. [CrossRef]
75. Nota, D.J.G. Sediments of the western Guyana shelf. In *Report of Orinoco Shelf Expedition, 2. Mendedel*; Landbomvhogedrool: Wegeningen, The Netherlands, 1958; Volume 58, pp. 1–98.
76. Izzo, F.C.; Kratter, M.; Nevin, A.; Zendri, E. A Critical Review on the Analysis of Metal Soaps in Oil Paintings. *ChemistryOpen* **2021**, *10*, 904–921. [CrossRef]
77. López Ruíz, J.; Rodríguez Badiola, E. La región volcánica neógena del sudeste de España. *Cons. Super. Investig. Cient.* **1980**, *36*, 5–53.
78. López Ruíz, J.; Rodríguez Badiola, E.; Arroyo, A.; Coy-YII, R. Los óxidos de Fe-Ti de las Rocas Calco-alcalinas del sureste de España. *Estud. Geol.* **1984**, *40*, 269–279. [CrossRef]
79. Li, Y.-H.; Schoonmaker, J.E. Chemical Composition and Mineralogy of Marine Sediments. *Treatise Geochem.* **2003**, *7*, 1–35.
80. Liu, C.; Wang, W.; Wang, H.; Zhu, C.; Ren, B. A Review on Removal of Iron Impurities from Quartz Mineral. *Minerals* **2023**, *13*, 1128. [CrossRef]
81. Smołka-Danielowska, D.; Kądziołka-Gaweł, M.; Krzykawski, T. Chemical and mineral composition of furnace slags produced in the combustion process of hard coal. *Int. J. Environ. Sci. Technol.* **2019**, *16*, 5387–5396. [CrossRef]
82. Velazco, F. Shallow marine sediments in the bay of Callao, Perú. *Inst. Mar. Perú* **2011**, *26*, 75–82.
83. Chang, J.; Li, Y.; Lu, H. The Morphological Characteristics of Authigenic Pyrite Formed in Marine Sediments. *J. Mar. Sci. Eng.* **2022**, *10*, 1533. [CrossRef]
84. Burdige, D.J.; Komada, T. Iron redox cycling, sediment resuspension and role of sediments in low oxygen environments as sources of iron to wáter column. *Mar. Chem.* **2020**, *223*, 103793. [CrossRef]
85. Canfield, D.E.; Raiswell, R.; Bottrell, S. The Reactivity of Sedimentary iron minerals towards sufide. *Am. J. Sci.* **1992**, *292*, 659–683. [CrossRef]
86. Rickard, D. Kinetics and mechanism of pyrite formation at low temperatures. *Am. J. Sci.* **1975**, *275*, 636–652. [CrossRef]
87. Yücel, M.; Konovalov, S.K.; Moore, T.S.; Janzen, C.P.; Luther, G.W., III. Sulfur speciation in the upper Black Sea sediments. *Chem. Geol.* **2010**, *269*, 364–375. [CrossRef]
88. Ranganath, N.; Padhi, A.K.; Padhi, A.K.; Rai, A.K. Framboidal—Colloform—Recrystallised pyrite in the granitoids of Wahkyn area, West Khasi hills, Meghalaya. *J. Geol. Soc. India* **2009**, *74*, 591–596. [CrossRef]
89. Wei, H.; Algeo, T.J.; Yu, H.; Wang, J.; Guo, C.; Shi, G. Episodic euxinia in the Changhsingian (late Permian) of South China: Evidence from framboidal pyrite and geochemical data. *Sediment. Geol.* **2015**, *319*, 78–97. [CrossRef]
90. Liu, K.; Huang, F.; Gao, S.; Zhang, Z.; Ren, Y.; An, B. Morphology of framboidal pyrite and its textural evolution: Evidence from the Logatchev area, Mid-Atlantic Ridge. *Ore Geol. Rev.* **2022**, *141*, 104630. [CrossRef]
91. Raiswell, R.; Buckley, F.; Berner, R.A.; Anderson, T.F. Degree of pyritization of iron as a paleoenvironmental indicator of bottom-water oxygenation. *J. Sediment. Petrol.* **1988**, *58*, 812–819.
92. Wedepohl, K.H. The composition of the continental crust. *Geochem. Cosmochim. Acta* **1995**, *59*, 1217–1232. [CrossRef]
93. Robledo Ardila, P.A.; Álvarez-Alonso, R.; Árcega-Cabrera, F.; Durán Valsero, J.J.; Morales García, R.; Lamas-Cosío, E.; Oceguera-Vargas, I.; DelValls, A. Assessment and Review of Heavy Metals Pollution in Sediments of the Mediterranean Sea. *Appl. Sci.* **2024**, *14*, 1435. [CrossRef]